11-20-2007

Measurement of the $t\bar{t}$ production cross section in $p\bar{p}$ collisions at $\sqrt{s}$ = 1.96 TeV using kinematic characteristics of lepton + jets events

V. M. Abazov
Joint Institute for Nuclear Research, Dubna, Russia

Kenneth A. Bloom
University of Nebraska-Lincoln, kenbloom@unl.edu

Gregory R. Snow
University of Nebraska-Lincoln, gsnow1@unl.edu

D0 Collaboration

Measurement of the $t\bar{t}$ production cross section in $p\bar{p}$ collisions at $\sqrt{s} = 1.96$ TeV using kinematic characteristics of lepton + jets events

V. M. Abazov,[35] B. Abbott,[75] M. Abolins,[65] B. S. Acharya,[28] M. Adams,[51] T. Adams,[49] E. Aguilo,[5] S. H. Ahn,[30] M. Ahsan,[59] G. D. Alexeev,[35] G. Alkhazov,[39] A. Alton,[64,*] G. Alverson,[63] G. A. Alves,[2] M. Anastasoaie,[34] L. S. Ancu,[34] T. Andeen,[53] S. Anderson,[45] B. Andrieu,[16] M. S. Anzelc,[53] Y. Arnoud,[13] M. Arov,[60] M. Arthaud,[17] A. Askew,[49] B. Åsman,[40] A. C. S. Assis Jesus,[3] O. Atramentov,[49] C. Autermann,[20] C. Avila,[7] C. Ay,[23] F. Badaud,[12] A. Baden,[61] L. Bagby,[52] B. Baldin,[50] D. V. Bandurin,[59] S. Banerjee,[28] P. Banerjee,[28] E. Barberis,[63] A.-F. Barfuss,[14] P. Bargassa,[80] P. Baringer,[58] J. Barreto,[2] J. F. Bartlett,[50] U. Bassler,[16] D. Bauer,[43] S. Beale,[5] A. Bean,[58] M. Begalli,[3] M. Begel,[71] C. Belanger-Champagne,[40] L. Bellantoni,[50] A. Bellavance,[50] J. A. Benitez,[65] S. B. Beri,[26] G. Bernardi,[16] R. Bernhard,[22] L. Berntzon,[14] I. Bertram,[42] M. Besançon,[17] R. Beuselinck,[43] V. A. Bezzubov,[38] P. C. Bhat,[50] V. Bhatnagar,[26] C. Biscarat,[19] G. Blazey,[52] F. Blekman,[43] S. Blessing,[49] D. Bloch,[18] K. Bloom,[67] A. Boehnlein,[50] D. Boline,[62] T. A. Bolton,[59] G. Borissov,[42] K. Bos,[33] T. Bose,[77] A. Brandt,[78] R. Brock,[65] G. Brooijmans,[70] A. Bross,[50] D. Brown,[78] N. J. Buchanan,[49] D. Buchholz,[53] M. Buehler,[81] V. Buescher,[21] S. Burdin,[42,†] S. Burke,[45] T. H. Burnett,[82] C. P. Buszello,[43] J. M. Butler,[62] P. Calfayan,[24] S. Calvet,[14] J. Cammin,[71] S. Caron,[33] W. Carvalho,[3] B. C. K. Casey,[77] N. M. Cason,[55] H. Castilla-Valdez,[32] S. Chakrabarti,[17] D. Chakraborty,[52] K. M. Chan,[55] K. Chan,[5] A. Chandra,[48] F. Charles,[18] E. Cheu,[45] F. Chevallier,[13] D. K. Cho,[62] S. Choi,[31] B. Choudhary,[27] L. Christofek,[77] T. Christoudias,[43] S. Cihangir,[50] D. Claes,[67] C. Clément,[40] B. Clément,[18] Y. Coadou,[5] M. Cooke,[80] W. E. Cooper,[50] M. Corcoran,[80] F. Couderc,[17] M.-C. Cousinou,[14] S. Crépé-Renaudin,[13] D. Cutts,[77] M. Ćwiok,[29] H. da Motta,[2] A. Das,[62] G. Davies,[43] K. De,[78] S. J. de Jong,[34] P. de Jong,[33] E. De La Cruz-Burelo,[64] C. De Oliveira Martins,[3] J. D. Degenhardt,[64] F. Déliot,[17] M. Demarteau,[50] R. Demina,[71] D. Denisov,[50] S. P. Denisov,[38] S. Desai,[50] H. T. Diehl,[50] M. Diesburg,[50] A. Dominguez,[67] H. Dong,[72] L. V. Dudko,[37] L. Duflot,[15] S. R. Dugad,[28] D. Duggan,[49] A. Duperrin,[14] J. Dyer,[65] A. Dyshkant,[52] M. Eads,[67] D. Edmunds,[65] J. Ellison,[48] V. D. Elvira,[50] Y. Enari,[77] S. Eno,[61] P. Ermolov,[37] H. Evans,[54] A. Evdokimov,[73] V. N. Evdokimov,[38] A. V. Ferapontov,[59] T. Ferbel,[71] F. Fiedler,[24] F. Filthaut,[34] W. Fisher,[50] H. E. Fisk,[50] M. Ford,[44] M. Fortner,[52] H. Fox,[22] S. Fu,[50] S. Fuess,[50] T. Gadfort,[82] C. F. Galea,[34] E. Gallas,[50] E. Galyaev,[55] C. Garcia,[71] A. Garcia-Bellido,[82] V. Gavrilov,[36] P. Gay,[12] W. Geist,[18] D. Gelé,[18] C. E. Gerber,[51] Y. Gershtein,[49] D. Gillberg,[5] G. Ginther,[71] N. Gollub,[40] B. Gómez,[7] A. Goussiou,[55] P. D. Grannis,[72] H. Greenlee,[50] Z. D. Greenwood,[60] E. M. Gregores,[4] G. Grenier,[19] Ph. Gris,[12] J.-F. Grivaz,[15] A. Grohsjean,[24] S. Grünendahl,[50] M. W. Grünewald,[29] J. Guo,[72] F. Guo,[72] P. Gutierrez,[75] G. Gutierrez,[50] A. Haas,[70] N. J. Hadley,[61] P. Haefner,[24] S. Hagopian,[49] J. Haley,[68] I. Hall,[75] R. E. Hall,[47] L. Han,[6] K. Hanagaki,[50] P. Hansson,[40] K. Harder,[44] A. Harel,[71] R. Harrington,[63] J. M. Hauptman,[57] R. Hauser,[65] J. Hays,[43] T. Hebbeker,[20] D. Hedin,[52] J. G. Hegeman,[33] J. M. Heinmiller,[51] A. P. Heinson,[48] U. Heintz,[62] C. Hensel,[58] K. Herner,[72] G. Hesketh,[63] M. D. Hildreth,[55] R. Hirosky,[81] J. D. Hobbs,[72] B. Hoeneisen,[11] H. Hoeth,[25] M. Hohlfeld,[21] S. J. Hong,[30] R. Hooper,[77] S. Hossain,[75] P. Houben,[33] Y. Hu,[72] Z. Hubacek,[9] V. Hynek,[8] I. Iashvili,[69] R. Illingworth,[50] A. S. Ito,[50] S. Jabeen,[62] M. Jaffré,[15] S. Jain,[75] K. Jakobs,[22] C. Jarvis,[61] R. Jesik,[43] K. Johns,[45] C. Johnson,[70] M. Johnson,[50] A. Jonckheere,[50] P. Jonsson,[43] A. Juste,[50] D. Käfer,[20] S. Kahn,[73] E. Kajfasz,[14] A. M. Kalinin,[35] J. R. Kalk,[65] J. M. Kalk,[60] S. Kappler,[20] D. Karmanov,[37] J. Kasper,[62] P. Kasper,[50] I. Katsanos,[70] D. Kau,[49] R. Kaur,[26] V. Kaushik,[78] R. Kehoe,[79] S. Kermiche,[14] N. Khalatyan,[38] A. Khanov,[76] A. Kharchilava,[69] Y. M. Kharzheev,[35] D. Khatidze,[70] H. Kim,[31] T. J. Kim,[30] M. H. Kirby,[34] M. Kirsch,[20] B. Klima,[50] J. M. Kohli,[26] J.-P. Konrath,[22] M. Kopal,[75] V. M. Korablev,[38] B. Kothari,[70] A. V. Kozelov,[38] D. Krop,[54] A. Kryemadhi,[81] T. Kuhl,[23] A. Kumar,[69] S. Kunori,[61] A. Kupco,[10] T. Kurča,[19] J. Kvita,[8] F. Lacroix,[12] D. Lam,[55] S. Lammers,[70] G. Landsberg,[77] J. Lazoflores,[49] P. Lebrun,[19] W. M. Lee,[50] A. Leflat,[37] F. Lehner,[41] J. Lellouch,[16] V. Lesne,[12] J. Leveque,[45] P. Lewis,[43] J. Li,[78] Q. Z. Li,[50] L. Li,[48] S. M. Lietti,[4] J. G. R. Lima,[52] D. Lincoln,[50] J. Linnemann,[65] V. V. Lipaev,[38] R. Lipton,[50] Y. Liu,[6] Z. Liu,[5] L. Lobo,[43] A. Lobodenko,[39] M. Lokajicek,[10] A. Lounis,[18] P. Love,[42] H. J. Lubatti,[82] A. L. Lyon,[50] A. K. A. Maciel,[2] D. Mackin,[80] R. J. Madaras,[46] P. Mättig,[25] C. Magass,[20] A. Magerkurth,[64] N. Makovec,[15] P. K. Mal,[55] H. B. Malbouisson,[3] S. Malik,[67] V. L. Malyshev,[35] H. S. Mao,[50] Y. Maravin,[59] B. Martin,[13] R. McCarthy,[72] A. Melnitchouk,[66] A. Mendes,[14] L. Mendoza,[7] P. G. Mercadante,[4] M. Merkin,[37] K. W. Merritt,[50] J. Meyer,[21] A. Meyer,[20] M. Michaut,[17] T. Millet,[19] J. Mitrevski,[70] J. Molina,[3] R. K. Mommsen,[44] N. K. Mondal,[28] R. W. Moore,[5] T. Moulik,[58] G. S. Muanza,[19] M. Mulders,[50] M. Mulhearn,[70] O. Mundal,[21] L. Mundim,[3] E. Nagy,[14] M. Naimuddin,[50] M. Narain,[77] N. A. Naumann,[34] H. A. Neal,[64] J. P. Negret,[7] P. Neustroev,[39] H. Nilsen,[22] A. Nomerotski,[50] S. F. Novaes,[4] T. Nunnemann,[24] V. O'Dell,[50] D. C. O'Neil,[5] G. Obrant,[39] C. Ochando,[15] D. Onoprienko,[59] N. Oshima,[50] J. Osta,[55] R. Otec,[9] G. J. Otero y Garzón,[51] M. Owen,[44] P. Padley,[80] M. Pangilinan,[77] N. Parashar,[56] S.-J. Park,[71] S. K. Park,[30] J. Parsons,[70] R. Partridge,[77] N. Parua,[54] A. Patwa,[73] G. Pawloski,[80] B. Penning,[22] P. M. Perea,[48] K. Peters,[44]

Y. Peters,[25] P. Pétroff,[15] M. Petteni,[43] R. Piegaia,[1] J. Piper,[65] M.-A. Pleier,[21] P. L. M. Podesta-Lerma,[32,‡] V. M. Podstavkov,[50] Y. Pogorelov,[55] M.-E. Pol,[2] P. Polozov,[36] A. Pompo,[1] B. G. Pope,[65] A. V. Popov,[38] C. Potter,[5] W. L. Prado da Silva,[3] H. B. Prosper,[49] S. Protopopescu,[73] J. Qian,[64] A. Quadt,[21] B. Quinn,[66] A. Rakitine,[42] M. S. Rangel,[2] K. J. Rani,[28] K. Ranjan,[27] P. N. Ratoff,[42] P. Renkel,[79] S. Reucroft,[63] P. Rich,[44] M. Rijssenbeek,[72] I. Ripp-Baudot,[18] F. Rizatdinova,[76] S. Robinson,[43] R. F. Rodrigues,[3] C. Royon,[17] P. Rubinov,[50] R. Ruchti,[55] G. Safronov,[36] G. Sajot,[13] A. Sánchez-Hernández,[32] M. P. Sanders,[16] A. Santoro,[3] G. Savage,[50] L. Sawyer,[60] T. Scanlon,[43] D. Schaile,[24] R. D. Schamberger,[72] Y. Scheglov,[39] H. Schellman,[53] P. Schieferdecker,[24] T. Schliephake,[25] C. Schmitt,[25] C. Schwanenberger,[44] A. Schwartzman,[68] R. Schwienhorst,[65] J. Sekaric,[49] S. Sengupta,[49] H. Severini,[75] E. Shabalina,[51] M. Shamim,[59] V. Shary,[17] A. A. Shchukin,[38] R. K. Shivpuri,[27] D. Shpakov,[50] V. Siccardi,[18] V. Simak,[9] V. Sirotenko,[50] P. Skubic,[75] P. Slattery,[71] D. Smirnov,[55] R. P. Smith,[50] J. Snow,[74] G. R. Snow,[67] S. Snyder,[73] S. Söldner-Rembold,[44] L. Sonnenschein,[16] A. Sopczak,[42] M. Sosebee,[78] K. Soustruznik,[8] M. Souza,[2] B. Spurlock,[78] J. Stark,[13] J. Steele,[60] V. Stolin,[36] A. Stone,[51] D. A. Stoyanova,[38] J. Strandberg,[64] S. Strandberg,[40] M. A. Strang,[69] M. Strauss,[75] E. Strauss,[72] R. Ströhmer,[24] D. Strom,[53] M. Strovink,[46] L. Stutte,[50] S. Sumowidagdo,[49] P. Svoisky,[55] A. Sznajder,[3] M. Talby,[14] P. Tamburello,[45] A. Tanasijczuk,[1] W. Taylor,[5] P. Telford,[44] J. Temple,[45] B. Tiller,[24] F. Tissandier,[12] M. Titov,[17] V. V. Tokmenin,[35] M. Tomoto,[50] T. Toole,[61] I. Torchiani,[22] T. Trefzger,[23] D. Tsybychev,[72] B. Tuchming,[17] C. Tully,[68] P. M. Tuts,[70] R. Unalan,[65] S. Uvarov,[39] L. Uvarov,[39] S. Uzunyan,[52] B. Vachon,[5] P. J. van den Berg,[33] B. van Eijk,[33] R. Van Kooten,[54] W. M. van Leeuwen,[33] N. Varelas,[51] E. W. Varnes,[45] A. Vartapetian,[78] I. A. Vasilyev,[38] M. Vaupel,[25] P. Verdier,[19] L. S. Vertogradov,[35] M. Verzocchi,[50] F. Villeneuve-Seguier,[43] P. Vint,[43] J.-R. Vlimant,[16] P. Vokac,[9] E. Von Toerne,[59] M. Voutilainen,[67,§] M. Vreeswijk,[33] R. Wagner,[68] H. D. Wahl,[49] L. Wang,[61] M. H. L. S Wang,[50] J. Warchol,[55] G. Watts,[82] M. Wayne,[55] M. Weber,[50] G. Weber,[23] H. Weerts,[65] A. Wenger,[22,‖] N. Wermes,[21] M. Wetstein,[61] A. White,[78] D. Wicke,[25] G. W. Wilson,[58] S. J. Wimpenny,[48] M. Wobisch,[60] D. R. Wood,[63] T. R. Wyatt,[44] Y. Xie,[77] S. Yacoob,[53] R. Yamada,[50] M. Yan,[61] T. Yasuda,[50] Y. A. Yatsunenko,[35] K. Yip,[73] H. D. Yoo,[77] S. W. Youn,[53] J. Yu,[78] C. Yu,[13] A. Yurkewicz,[72] A. Zatserklyaniy,[52] C. Zeitnitz,[25] D. Zhang,[50] T. Zhao,[82] B. Zhou,[64] J. Zhu,[72] M. Zielinski,[71] D. Zieminska,[54] A. Zieminski,[54] L. Zivkovic,[70] V. Zutshi,[52] and E. G. Zverev[37]

(D0 Collaboration)

[1]*Universidad de Buenos Aires, Buenos Aires, Argentina*
[2]*LAFEX, Centro Brasileiro de Pesquisas Físicas, Rio de Janeiro, Brazil*
[3]*Universidade do Estado do Rio de Janeiro, Rio de Janeiro, Brazil*
[4]*Instituto de Física Teórica, Universidade Estadual Paulista, São Paulo, Brazil*
[5]*University of Alberta, Edmonton, Alberta, Canada, Simon Fraser University, Burnaby, British Columbia, Canada, York University, Toronto, Ontario, Canada, and McGill University, Montreal, Quebec, Canada*
[6]*University of Science and Technology of China, Hefei, People's Republic of China*
[7]*Universidad de los Andes, Bogotá, Colombia*
[8]*Center for Particle Physics, Charles University, Prague, Czech Republic*
[9]*Czech Technical University, Prague, Czech Republic*
[10]*Center for Particle Physics, Institute of Physics, Academy of Sciences of the Czech Republic, Prague, Czech Republic*
[11]*Universidad San Francisco de Quito, Quito, Ecuador*
[12]*Laboratoire de Physique Corpusculaire, IN2P3-CNRS, Université Blaise Pascal, Clermont-Ferrand, France*
[13]*Laboratoire de Physique Subatomique et de Cosmologie, IN2P3-CNRS, Universite de Grenoble 1, Grenoble, France*
[14]*CPPM, IN2P3-CNRS, Université de la Méditerranée, Marseille, France*
[15]*Laboratoire de l'Accélérateur Linéaire, IN2P3-CNRS et Université Paris-Sud, Orsay, France*
[16]*LPNHE, IN2P3-CNRS, Universités Paris VI and VII, Paris, France*
[17]*DAPNIA/Service de Physique des Particules, CEA, Saclay, France*
[18]*IPHC, Université Louis Pasteur et Université de Haute Alsace, CNRS, IN2P3, Strasbourg, France*
[19]*IPNL, Université Lyon 1, CNRS/IN2P3, Villeurbanne, France and Université de Lyon, Lyon, France*
[20]*III. Physikalisches Institut A, RWTH Aachen, Aachen, Germany*
[21]*Physikalisches Institut, Universität Bonn, Bonn, Germany*
[22]*Physikalisches Institut, Universität Freiburg, Freiburg, Germany*
[23]*Institut für Physik, Universität Mainz, Mainz, Germany*
[24]*Ludwig-Maximilians-Universität München, München, Germany*
[25]*Fachbereich Physik, University of Wuppertal, Wuppertal, Germany*
[26]*Panjab University, Chandigarh, India*
[27]*Delhi University, Delhi, India*
[28]*Tata Institute of Fundamental Research, Mumbai, India*

[29]*University College Dublin, Dublin, Ireland*
[30]*Korea Detector Laboratory, Korea University, Seoul, Korea*
[31]*SungKyunKwan University, Suwon, Korea*
[32]*CINVESTAV, Mexico City, Mexico*
[33]*FOM-Institute NIKHEF and University of Amsterdam/NIKHEF, Amsterdam, The Netherlands*
[34]*Radboud University Nijmegen/NIKHEF, Nijmegen, The Netherlands*
[35]*Joint Institute for Nuclear Research, Dubna, Russia*
[36]*Institute for Theoretical and Experimental Physics, Moscow, Russia*
[37]*Moscow State University, Moscow, Russia*
[38]*Institute for High Energy Physics, Protvino, Russia*
[39]*Petersburg Nuclear Physics Institute, St. Petersburg, Russia*
[40]*Lund University, Lund, Sweden, Royal Institute of Technology and Stockholm University, Stockholm, Sweden, and Uppsala University, Uppsala, Sweden*
[41]*Physik Institut der Universität Zürich, Zürich, Switzerland*
[42]*Lancaster University, Lancaster, United Kingdom*
[43]*Imperial College, London, United Kingdom*
[44]*University of Manchester, Manchester, United Kingdom*
[45]*University of Arizona, Tucson, Arizona 85721, USA*
[46]*Lawrence Berkeley National Laboratory and University of California, Berkeley, California 94720, USA*
[47]*California State University, Fresno, California 93740, USA*
[48]*University of California, Riverside, California 92521, USA*
[49]*Florida State University, Tallahassee, Florida 32306, USA*
[50]*Fermi National Accelerator Laboratory, Batavia, Illinois 60510, USA*
[51]*University of Illinois at Chicago, Chicago, Illinois 60607, USA*
[52]*Northern Illinois University, DeKalb, Illinois 60115, USA*
[53]*Northwestern University, Evanston, Illinois 60208, USA*
[54]*Indiana University, Bloomington, Indiana 47405, USA*
[55]*University of Notre Dame, Notre Dame, Indiana 46556, USA*
[56]*Purdue University Calumet, Hammond, Indiana 46323, USA*
[57]*Iowa State University, Ames, Iowa 50011, USA*
[58]*University of Kansas, Lawrence, Kansas 66045, USA*
[59]*Kansas State University, Manhattan, Kansas 66506, USA*
[60]*Louisiana Tech University, Ruston, Louisiana 71272, USA*
[61]*University of Maryland, College Park, Maryland 20742, USA*
[62]*Boston University, Boston, Massachusetts 02215, USA*
[63]*Northeastern University, Boston, Massachusetts 02115, USA*
[64]*University of Michigan, Ann Arbor, Michigan 48109, USA*
[65]*Michigan State University, East Lansing, Michigan 48824, USA*
[66]*University of Mississippi, University, Mississippi 38677, USA*
[67]*University of Nebraska, Lincoln, Nebraska 68588, USA*
[68]*Princeton University, Princeton, New Jersey 08544, USA*
[69]*State University of New York, Buffalo, New York 14260, USA*
[70]*Columbia University, New York, New York 10027, USA*
[71]*University of Rochester, Rochester, New York 14627, USA*
[72]*State University of New York, Stony Brook, New York 11794, USA*
[73]*Brookhaven National Laboratory, Upton, New York 11973, USA*
[74]*Langston University, Langston, Oklahoma 73050, USA*
[75]*University of Oklahoma, Norman, Oklahoma 73019, USA*
[76]*Oklahoma State University, Stillwater, Oklahoma 74078, USA*
[77]*Brown University, Providence, Rhode Island 02912, USA*
[78]*University of Texas, Arlington, Texas 76019, USA*
[79]*Southern Methodist University, Dallas, Texas 75275, USA*
[80]*Rice University, Houston, Texas 77005, USA*
[81]*University of Virginia, Charlottesville, Virginia 22901, USA*

[*]Visitor from Augustana College, Sioux Falls, SD, USA.
[†]Visitor from The University of Liverpool, Liverpool, United Kingdom.
[‡]Visitor from ICN-UNAM, Mexico City, Mexico.
[§]Visitor from Helsinki Institute of Physics, Helsinki, Finland.
[‖]Visitor from Universität Zürich, Zürich, Switzerland.

[82]*University of Washington, Seattle, Washington 98195, USA*
(Received 25 May 2007; published 27 November 2007)

We present a measurement of the top quark pair production cross section in $p\bar{p}$ collisions at $\sqrt{s} = 1.96$ TeV utilizing 425 pb^{-1} of data collected with the D0 detector at the Fermilab Tevatron Collider. We consider the final state of the top quark pair containing one high-p_T electron or muon and at least four jets. We exploit specific kinematic features of $t\bar{t}$ events to extract the cross section. For a top quark mass of 175 GeV, we measure $\sigma_{t\bar{t}} = 6.4^{+1.3}_{-1.2}(\text{stat}) \pm 0.7(\text{syst}) \pm 0.4(\text{lum})$ pb, in good agreement with the standard model prediction.

DOI: 10.1103/PhysRevD.76.092007 PACS numbers: 13.85.Lg, 13.85.Qk, 14.65.Ha

I. INTRODUCTION

Since the discovery of the top quark in 1995 by the CDF and D0 experiments [1], the Fermilab Tevatron $p\bar{p}$ Collider with its center-of-mass energy of $\sqrt{s} = 1.96$ TeV is still the only collider where top quarks can be studied. Within the standard model, top quarks are produced either in pairs via strong interactions or as single top events via electroweak interactions with a lower expected cross section [2]. Evidence for the latter production mode has been recently found by the D0 collaboration [3]. At the current Tevatron Collider center-of-mass energy, top quark pair production is predicted to occur via $q\bar{q}$ annihilation (85%) or gluon fusion (15%).

The $t\bar{t}$ pair production cross section was measured in various channels during Run I of the Fermilab Tevatron Collider at a center-of-mass energy of $\sqrt{s} = 1.8$ TeV [4]. The precision of these measurements was severely limited by available statistics. The 10% higher collision energy of the current Tevatron Collider run leads to a 30% higher expected top quark pair production rate; together with an increased luminosity, the precision on measurements of the top quark production and decay properties can therefore be substantially increased. The latest theoretical calculations [5–7] of the $t\bar{t}$ production cross section at next-to-leading order (NLO) have an uncertainty ranging from 9% to 12%. Recent measurements with a data set approximately twice as large as in Run I [8,9] are consistent with these predictions within the uncertainties.

Deviations from the standard model could occur due to the presence of new physics, such as resonant $t\bar{t}$ production [10], a novel top quark decay mechanism, as, for example, $t \to H^+ b$ [11] or a similar final-state signature from a toplike particle [12]. Some of these effects could cause the inclusive $t\bar{t}$ cross section ($\sigma_{t\bar{t}}$) to be different from the standard model prediction. Others could cause differences in top decay branching fractions, thus leading to $\sigma_{t\bar{t}}$ measured in different decay channels to disagree with the expectations computed using the standard model branching fractions. Therefore measurements of $\sigma_{t\bar{t}}$ in different top quark decay channels and using different analysis methods complement each other.

In this paper we present a new measurement of the top quark production cross section in the ℓ + jets channel, where one of the W bosons decays hadronically, and the other one leptonically into an electron ($W \to e\nu$) or a muon ($W \to \mu\nu$). W boson decays into a τ lepton with a subsequent decay of the latter into an electron or a muon are included in the signal sample. Each of the two decay channels represent approximatively 17% of the total top quark pair production and decay. We exploit the kinematic properties of the events to separate $t\bar{t}$ signal from W + jets background, instead of the often-exploited requirement of a final-state separated vertex that is consistent with the b decay. This choice makes this measurement less dependent on the assumption that a top quark decays into a b quark.

The measurement is based on a data sample taken between August 2002 and August 2004 with an integrated luminosity of 425 pb^{-1}, which represents approximatively a factor two increase with respect to the previously published measurement by the D0 experiment [8].

After a short description of the relevant D0 detector parts and underlying object identification algorithms, we describe the data and Monte Carlo samples, the event selection, the background determination, and the procedure to extract the top quark signal. Finally, we discuss the systematic uncertainties associated with the cross section measurement.

II. D0 DETECTOR

The D0 detector [13] is a nearly hermetic multipurpose apparatus built to investigate $p\bar{p}$ interactions at high transverse momentum. The measurements reported here rely on the tracking system, the Uranium-Liquid Argon calorimeter, the muon spectrometer, and the luminosity detectors, which are briefly described below. The coordinate system is right-handed with the z axis along the Tevatron proton beam direction, the y axis vertical, and the x axis pointing outside of the accelerator ring. The coordinates are also expressed in terms of the azimuthal angle φ, rapidity y, and pseudorapidity η. The latter are defined as functions of the polar angle θ as $y(\theta, \beta) \equiv \frac{1}{2}\ln[(1 + \beta\cos\theta)/(1 - \beta\cos\theta)]$; $\eta(\theta) \equiv y(\theta, 1)$, where β is the ratio of particle momentum to its energy. When the center of the D0 detector is considered as the origin of the coordinate system, these coordinates are referred to as detector coordinates φ_{det} and η_{det}; when the reconstructed interaction vertex is considered as the origin of the coordinate system,

these coordinates are referred to as physics coordinates φ and η.

The tracking system includes the silicon microstrip tracker (SMT) and the central fiber tracker (CFT). A superconducting solenoid surrounds the tracking system and provides a uniform magnetic field of 2 T. The SMT is a system closest to the beam pipe. It has six barrels in the central region of $|\eta_{\rm det}| < 1.5$, each barrel is 12 cm long and capped at high $|z|$ by a disk with an external radius of 10.5 cm. Each barrel has four silicon readout layers, composed of two staggered and overlapping sublayers. Each small-radius disk is composed of 12 double-sided wedge-shaped detectors. Track reconstruction in the forward region up to $|\eta_{\rm det}| < 3$ is provided by two units composed of three small and two large radius disks located at $|z| = 44.8$, 49.8, 54.8 cm and 110, 120 cm, respectively. Large radius disks are composed of 48 single-sided wedges with an external radius of 26 cm. The CFT consists of 8 concentric cylinders and covers the radial space from 20 to 52 cm. The two innermost cylinders are 1.66 m long, and the outer six cylinders are 2.52 m long. Each cylinder supports two doublets of overlapping scintillating fibers with the diameter of 0.84 mm, one doublet being parallel to the beam axis, the other with an alternating stereo angle of $\pm 3^\circ$. Light signals are transferred via clear optical fibers to solid-state visible light photon counters (VLPCs) that have a quantum efficiency of about 80%. Tracks are reconstructed combining the hits from both tracking detectors.

The calorimeter is used to reconstruct jets, electrons, photons, and missing transverse energy of noninteracting particles such as neutrinos. The D0 Uranium-Liquid Argon calorimeter which surrounds the tracking system is divided into the central calorimeter (CC) up to $|\eta_{\rm det}| \simeq 1.0$ and two endcap calorimeters (EC) extending the coverage to $|\eta_{\rm det}| \simeq 4.0$, housed in separate cryostats. Each calorimeter consists of an electromagnetic section with depleted Uranium absorber plates, a fine hadronic section with Uranium-Niobium absorbers, and a coarse hadronic section with Copper (stainless steel) absorbers in the CC (EC). The calorimeter is compact and highly segmented in the transverse and the longitudinal directions with about 56 000 channels in total. In φ, the electromagnetic part is divided into 64 modules and the hadronic part into 32 modules. The electromagnetic part has a depth of about 20 radiation lengths (X_0); and with the hadronic sections, the calorimeter has a total of 7.2 nuclear interaction lengths (λ_I) at $\eta = 0$ and of $10.3\lambda_I$ at $|\eta| \simeq 4$. The intercryostat region is equipped with scintillation detectors (intercryostat detectors or ICD) to improve energy resolution.

The muon system is the outermost part of the D0 detector. It consists of three layers of tracking detectors used for precise coordinate measurements and triggering and two layers of scintillation counters used for triggering [14]. Proportional drift tubes (PDT) cover the central region ($|\eta_{\rm det}| < 1.0$), and mini drift tubes (MDT) extend the coverage to $|\eta_{\rm det}| = 2.0$. One layer of scintillation counters in the central region and two layers in the forward region ($1.0 < |\eta_{\rm det}| < 2.0$) along with two layers of drift tubes (B and C layers) are located outside of a 1.8T iron toroid while the innermost layers (A) of muon tracking detectors and scintillators are located in front of it. The support structure underneath the D0 detector allows only for partial coverage in this region.

The luminosity is determined from the rate of inelastic collisions measured by the luminosity monitors (LM) located in front of the ECs at $z = \pm 140$ cm. The LM consists of two arrays of 24 plastic scintillator counters with photomultiplier readout and covers the pseudorapidity range $|\eta_{\rm det}|$ between 2.7 and 4.4. The uncertainty on the luminosity measurement is $\pm 6.1\%$ [15] and is dominated by the uncertainty on the $p\bar{p}$ inelastic cross section.

III. OBJECT IDENTIFICATION

A. Primary vertex

The primary (or hard scatter) vertex of the event is reconstructed in three steps. At the first step, we locate a beam spot position using reconstructed tracks with the transverse momentum of $p_T > 0.5$ GeV. These tracks should have at least two hits in the SMT detector and the significance of the distance of closest approach $S_{\rm dca} = |dca/\sigma_{\rm dca}| < 100$. The distance of closest approach (dca) is calculated with respect to the center of the detector in the plane transverse to the beam line. At the second step, we impose a more stringent requirement on the tracks, $S_{\rm dca} < 3$, where $S_{\rm dca}$ is calculated with respect to the beam spot determined in the previous step. These tracks are then used to fit the final primary vertices. We use information on the position of these tracks along the beam line to identify tracks belonging to different interactions and build clusters of the tracks within 2 cm from each other. All tracks in each cluster are fitted to a common vertex using the Kalman filter technique [16]. Finally, to distinguish the position of the hard scatter interaction from the simultaneously produced minimum bias scatters, a minimum bias probability is computed for each reconstructed vertex based on the transverse momenta and the total number of associated tracks. The primary vertex with the lowest minimum bias probability is selected as the hard scatter.

The primary vertex finding algorithm reconstructs vertices in the fiducial region of the SMT with an efficiency close to 100%. The position resolution, measured in data as a difference between the reconstructed vertex position and the position of the beam spot center, depends on the number of tracks fitted to the primary vertex and is around 40 μm in the plane transverse to the beam direction. It is dominated by the beam spot size of about 30 μm.

For the analysis, we select events with the primary vertex within the SMT fiducial region $|z_{\rm PV}| \leq 60$ cm and at least three tracks attached to the vertex.

B. Electrons

The electron identification is based on clusters of calorimeter cells found in the CC within $|\eta_{\rm det}| < 1.1$ using a simple cone algorithm with a cone size of $\mathcal{R} = \sqrt{(\Delta\eta)^2 + (\Delta\varphi)^2} = 0.2$. A cluster is considered a "loose" electron if (i) at least 90% of its reconstructed energy is in the electromagnetic part of the calorimeter ($f_{\rm EM} > 0.9$), (ii) the cluster is isolated, (iii) its shower shape is consistent with an electromagnetic shower, and (iv) there is at least one track in a $\Delta\eta \times \Delta\varphi$ road of size 0.05×0.05 around the cluster. The angular coordinates η, φ of the electron are taken from the parameters of the matched track; its energy is determined from the calorimeter cluster. The isolation criterion $f_{\rm iso}$ requires the ratio of the difference of the total energy within the cone size $\mathcal{R} < 0.4$ around the center of the cluster and the energy deposited in electromagnetic layers within the cone size $\mathcal{R} < 0.2$ to the reconstructed electron energy not to exceed 15%.

The electron shower-shape estimator is built from seven observables characterizing the electron shower shapes, which are the energy deposits in the first five layers of the calorimeter, the azimuthal extension of the cluster in the finely segmented third layer of the calorimeter, and the logarithm of the cluster total energy. From these observables a covariance matrix is built, where the matrix elements are computed from reference Monte Carlo samples at different cluster energies and pseudorapidities. The covariance parameter χ^2_H measures the consistency of a given shower to be an electromagnetic one. As the observables are not normally distributed, χ^2_H does not follow a normal χ^2 distribution and a cut on $\chi^2_H < 50$ is applied for electrons.

To define a "tight" electron we combine in a likelihood discriminant the variables defined above ($f_{\rm EM}$, χ^2_H) with (i) the ratio of the transverse component of the cluster energy measured in the calorimeter to the transverse momentum of the matched track, $E_T^{\rm cal}/p_T^{\rm track}$, (ii) the χ^2 probability of a track matched to the calorimeter cluster, (iii) the dca of the matched track with respect to the primary vertex, (iv) the number of tracks within a cone of $\mathcal{R} = 0.05$ around the matched track, and (v) the sum of transverse momenta of the tracks inside a cone of $\mathcal{R} < 0.4$ around, but excluding the candidate track. By construction, a discriminant value close to unity corresponds to a prompt isolated electron. We require that tight electrons satisfy the loose criteria and have a likelihood discriminant $\mathcal{L}_{\rm em} > 0.85$.

The electron energy scale is fixed by comparing the di-electron invariant mass distribution in $Z \to ee$ events selected from the data with the simulated expectation based on a Z boson mass of 91.19 GeV [17]. Additional random smearing is applied to the simulated electron energy to tune the resolution to that observed in the data.

C. Muons

Muons are identified from tracks reconstructed in the layers of the muon system and matched to a track reconstructed in the central tracking system taking advantage of its superior momentum and position resolution. For this analysis, we accept muons having (i) at least two wire hits and at least one scintillator hit in both the A layer inside the toroid and the B and C layers outside, (ii) three matched reconstructed muon track segments from all three muon system tracking layers, (iii) a good quality matched track in the central tracking system ($\chi^2/N_{\rm dof} < 4$), and (iv) consistency originating from the primary interaction vertex. The last condition includes the requirements that the timing of the muon, determined from associated scintillator hits, has to be within 10 ns of the beam interaction time, that the smallest distance along z axis between the primary vertex and the muon track must be less than 1 cm and $S_{\rm dca} < 3$.

Muons are distinguished as loose and tight depending on their isolation with respect to other reconstructed objects in the event. The loose muon isolation criterion is defined by demanding that a muon is separated from a jet by $\Delta\mathcal{R}(\mu, \text{jet}) > 0.5$ where $\Delta\mathcal{R}$ is the distance in pseudorapidity-azimuthal angle space. For a tight muon identification, the muon is additionally required to be isolated from energy depositions in the calorimeter and additional tracks in the tracking system. The calorimeter isolation requires the sum of the calorimeter cells' transverse energies between two cones of radius $\mathcal{R} = 0.1$ and $\mathcal{R} = 0.4$ around the muon track to be smaller than 8% of the muon p_T. The track isolation is based on the sum of the tracks' momenta contained in a cone of $\mathcal{R} = 0.5$ around the muon track, excluding the muon track itself. We require the sum to be less than 6% of the muon p_T.

The muon momentum is measured from the matched reconstructed central track. Because of the limited acceptance of the SMT some tracks have hits in the CFT part of the central tracking system only, and therefore their resolution is degraded. To improve the momentum resolution of such tracks we apply a correction to the inverse track transverse momentum. It is based on a fit constraining the track dca to zero with respect to the primary vertex in the transverse plane.

The muon momentum scale is fixed by comparing the di-muon invariant mass distribution in $Z \to \mu\mu$ events selected from the data with the simulated expectation based on the Z boson mass. Additional random smearing of the muon transverse momenta is performed to tune the simulated muon momentum resolution to that observed in the data.

D. Jets

Jets are reconstructed from calorimeter cells using the iterative, seed-based cone algorithm including midpoints [18] with a cone radius of $\mathcal{R}_{\rm jet} = \sqrt{(\Delta y)^2 + (\Delta\varphi)^2} = 0.5$.

The minimum p_T of a reconstructed jet is required to be 8 GeV before any energy corrections are applied. To remove jets resulting from noise in the calorimeter or created by electromagnetic particles, further quality criteria are applied: (i) the jet has to have between 5% and 95% of its reconstructed energy in the electromagnetic calorimeter and less than 40% of its energy in the outermost hadronic section of the calorimeter, (ii) the ratio of the highest to the next-to-highest transverse momentum cell in a jet has to be less than 10, (iii) a single calorimeter tower must not contain more than 90% of the jet energy, and (iv) the jet has to be confirmed by the independent calorimeter trigger readout.

Previously reconstructed electrons and photons might also be reconstructed as jets in the calorimeter. To avoid the resulting double counting, we reject any jet overlapping with an electromagnetic object within a cone of $\mathcal{R} < 0.5$ fulfilling the electron identification criteria (i)–(iii) of Sec. III B and having $p_T > 15$ GeV and $|\eta_{\text{det}}| < 2.5$.

We correct the p_T of each reconstructed jet to the particle level by applying jet energy scale (JES) corrections [19]. These corrections account for imperfect calorimeter response, the jet energy offset due to the underlying event, multiple interactions, pile-up effects and noise, and the jet energy loss due to showering outside of the fixed-size jet cone. We make use of transverse momentum conservation in a sample of photon + jet events to calibrate the jet energy and determine the jet energy scale corrections separately for data and simulation. Since the jet identification efficiency and energy resolution differ between data and simulation, the jet transverse momenta are smeared and depending on the jet $|\eta_{\text{det}}|$ from 1% to 3% of the jets are removed to reproduce the data.

E. Missing E_T

The presence of a neutrino in the final state can be inferred from the energy imbalance of an event in the transverse plane. It is reconstructed from the vector sum of the transverse energies of all cells surviving various noise suppression algorithms and not belonging to a coarse hadronic section of the calorimeter. The latter cells are generally excluded due to their higher noise level. They are, however, included if clustered within jets. The vector opposite to this total visible momentum vector is referred to as a raw missing transverse energy vector.

The calorimeter response to electromagnetic particles such as photons, electrons, or π^0s is different from that due to hadrons and, in particular, from that due to jets. In events with both electromagnetic objects and jets, this imbalance propagates directly into missing transverse energy ($\not\!\!E_T$). As a JES correction is derived for all jets satisfying criteria (i)–(iv) of Sec. III D, it also has to be applied to $\not\!\!E_T$. In order to do so, the JES correction (limited to the response part) applied to jets is subtracted from the $\not\!\!E_T$ vector. In an equivalent way the EM correction for electromagnetic objects is applied to the $\not\!\!E_T$ vector.

Muons are minimum ionizing particles throughout the entire detector. Hence they will deposit only a small amount of energy in the calorimeter and their presence can thus fake missing transverse energy. Therefore we replace the transverse energy deposited by muons, satisfying requirements (i)–(iii) of Sec. III C, in the calorimeter by the transverse momentum measured by the tracking system.

IV. DATA SAMPLES AND MONTE CARLO SIMULATION

A. Event trigger

The D0 trigger is based on a three-level pipeline system. The first level consists of hardware and firmware components that make a trigger decision based on fast signal inputs from the luminosity monitor, the tracking system, the calorimeter, and the muon system. The second level combines the same information to construct simple physics objects, whereas the third level is software based and uses the full event information obtained with a simplified reconstruction. The accepted event rates are 2 kHz, 1 kHz, and 50 Hz, respectively, for level 1 (L1), level 2 (L2), and level 3 (L3). For all events used in this analysis the trigger system is required to find at least one jet and an electron or muon.

The D0 calorimeter trigger is based on energy deposited in towers of calorimeter cells with a transverse granularity of $\Delta\eta \times \Delta\varphi = 0.2 \times 0.2$. In addition, towers are segmented longitudinally into electromagnetic (EM) and hadronic (HAD) sections. The level 1 electron trigger requires a minimum transverse energy (E_T) deposition in the electromagnetic section of a tower. At level 2, a seed-based cluster algorithm sums the energy in neighboring towers and bases the trigger decision on the E_T and the electromagnetic fraction (f_{EM}) of a cluster. At level 3, the electron identification is based on a simple cone algorithm with $\mathcal{R} < 0.25$ and the trigger decision is based on the requirements on E_T, f_{EM} and a shower-shape estimator.

The level 1 jet trigger is based on the E_T deposited in a full calorimeter trigger tower. At level 2, these towers are summed by a seed-based cluster algorithm within a 5×5 tower array. The level 3 jet algorithm uses a simple cone algorithm with $\mathcal{R} < 0.5$ or $\mathcal{R} < 0.7$ and a decision is taken based on the E_T within the cone.

The level 1 muon trigger is based on input from the muon scintillator counters, the muon wire chambers, and the track trigger system. At level 2, muons are reconstructed from the muon scintillator and wire chamber information and requirements on the number of muons, their transverse momentum p_T and position in η as well as on their quality can be made. The quality is based on the number of scintillators and wires hit. At level 3, muon tracks are fitted using information from the tracking and muon systems. This refines the selection in p_T, η, and reconstruction quality.

The data used for the measurement presented in this paper were collected between August 2002 and August 2004 and correspond to an integrated luminosity of 422 ± 26 pb^{-1} in the μ + jets and 425 ± 26 pb^{-1} in the e + jets channel, respectively [15]. The trigger criteria evolved over this period of time to account for the increase in instantaneous luminosity while keeping a constant trigger rate. The different trigger criteria and the corresponding integrated luminosity collected are summarized in Table I for the e + jets and the μ + jets data.

B. Trigger efficiency

Only a fraction of all produced $t\bar{t}$ events will pass the selection criteria imposed by the trigger system. The trigger efficiency for $t\bar{t}$ events is estimated by folding into simulated events the per-lepton and per-jet probability to satisfy the individual trigger conditions at L1, L2, and L3. The total probability for an event to satisfy a set of trigger requirements is obtained assuming that the probability for a single object, described below, to satisfy a specific trigger condition is independent of the presence of other objects in the event. Under this assumption, the contributions from the lepton and the jets to the total event probability factorize, so that

$$P_{\text{event}} = P_{\text{lepton}} \times P_{\text{jet}}. \quad (1)$$

Furthermore, under the assumption of independent trigger objects, the probability P_{jet} for at least one out of N_{jet} jets in the event to fulfill the jet part of the trigger requirement is given by

$$P_{\text{jet}} = 1 - \prod_{i=1}^{N_{\text{jet}}}(1 - P_i), \quad (2)$$

where P_i is the probability for one jet to pass the trigger conditions.

The total trigger efficiency is then calculated as the luminosity-weighted average of the event probability associated to the trigger requirements corresponding to each data-taking period.

C. Trigger efficiency measurement

The probability for a lepton or a jet to satisfy a particular trigger requirement is measured in samples of events that are unbiased with respect to the trigger requirement under study. Reconstructed leptons or jets are identified in the event offline and the trigger efficiency is determined by measuring the fraction of objects satisfying the trigger condition under study. These efficiencies are generally parametrized as a function of the object p_T and η_{det}.

We use a sample of $Z \to e^+e^-$ ($Z \to \mu^+\mu^-$) events to calculate the fraction of electrons (muons), fulfilling the requirements defined in Sec. III B and III C, that pass the trigger requirement under study. We selected events triggered by a single electron (muon) trigger and require the presence of two reconstructed electrons (muons) fulfilling the tight selection criteria defined in Sec. III B (III C) for electrons (muons), respectively. The invariant mass of the two selected leptons is required to be within a window around the Z mass, $80\ \text{GeV} < M_{\ell\ell} < 100\ \text{GeV}$. We choose one electron (muon) as a ''tag'' and require it to have p_T above 20 GeV and to be matched to an electron (muon) object at all relevant trigger levels. We use the other ''probe'' electron (muon) to calculate the efficiency

TABLE I. Trigger requirements for different data-taking periods.

e + jets channel				
Trigger name	$\int \mathcal{L}dt$ (pb^{-1})	Level 1	Level 2	Level 3
EM15_2JT15	128	1 EM tower, $E_T > 10$ GeV 2 jet towers, $p_T > 5$ GeV	$1e$, $E_T > 10$ GeV, $f_{\text{EM}} > 0.85$ 2 jets, $E_T > 10$ GeV	1 tight e, $E_T > 15$ GeV 2 jets, $p_T > 15$ GeV
E1_SHT15_2J20	244	1 EM tower, $E_T > 11$ GeV	none	1 tight e, $E_T > 15$ GeV 2 jets, $p_T > 20$ GeV
E1_SHT15_2J_J25	53	1 EM tower, $E_T > 11$ GeV	1 EM cluster, $E_T > 15$ GeV	1 tight e, $E_T > 15$ GeV 2 jets, $p_T > 20$ GeV 1 jet, $p_T > 25$ GeV
μ + jets channel				
Trigger name	$\int \mathcal{L}dt$ (pb^{-1})	Level 1	Level 2	Level 3
MU_JT20_L2M0	132	1μ, $\lvert\eta\rvert < 2.0$ 1 jet tower, $p_T > 5$ GeV	1μ, $\lvert\eta\rvert < 2.0$	1 jet, $p_T > 20$ GeV
MU_JT25_L2M0	244	1μ, $\lvert\eta\rvert < 2.0$ 1 jet tower, $p_T > 3$ GeV	1μ, $\lvert\eta\rvert < 2.0$ 1 jet, $p_T > 10$ GeV	1 jet, $p_T > 25$ GeV
MUJ2_JT25	30	1μ, $\lvert\eta\rvert < 2.0$ 1 jet tower, $p_T > 5$ GeV	1μ, $\lvert\eta\rvert < 2.0$ 1 jet, $p_T > 8$ GeV	1 jet, $p_T > 25$ GeV
MUJ2_JT25_LM3	16	1μ, $\lvert\eta\rvert < 2.0$ 1 jet tower, $p_T > 5$ GeV	1μ, $\lvert\eta\rvert < 2.0$ 1 jet, $p_T > 8$ GeV	1μ, $\lvert\eta\rvert < 2.0$ 1 jet, $p_T > 25$ GeV

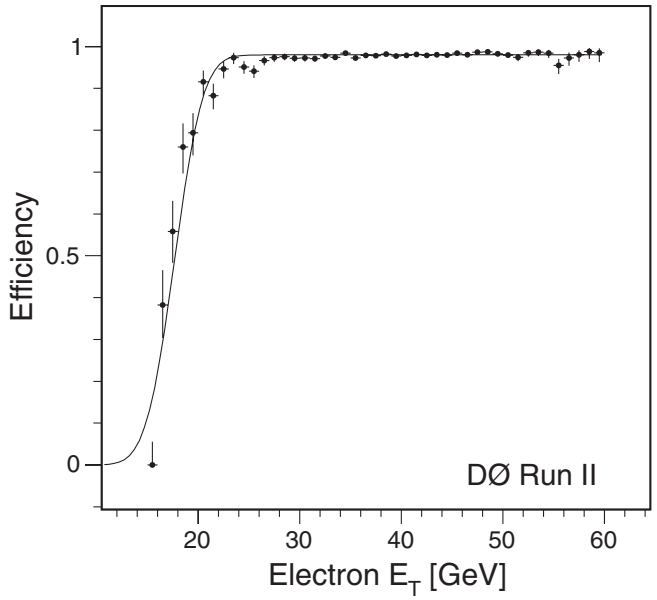

FIG. 1. Electron L3 trigger efficiency for the last data-taking period and its parametrization as a function of the electron E_T.

of the trigger criterion studied. If both leptons fulfill the tag requirements, each of them serves both as a tag and as a probe.

Figure 1 shows the measured probability that the electron passes the L3 condition and the parametrization used in the analysis for the last data-taking period. Figure 2 shows the measured muon trigger efficiencies for the first and second data-taking periods. The measured efficiency is parametrized as a function of the muon η_{det} with the fit function chosen to be symmetric in η_{det}. Both the muon detector geometry and the details of offline reconstruction contribute to the observed shape of the distribution. We do not use the dependence of the trigger efficiency on the muon transverse momentum in the parametrization. However, due to the spread of efficiencies observed, an overall uncertainty of $\pm 2\%$ is added in quadrature to the statistical fit uncertainty.

We measure jet trigger efficiencies in a sample of data events which fire one of the many muon triggers present in a set of triggers corresponding to a data-taking period of interest. The jet trigger efficiencies are parametrized as a function of jet p_T in three regions of the calorimeter: CC ($|\eta_{\text{det}}| < 0.8$), ICD ($0.8 \leq |\eta_{\text{det}}| < 1.5$), and EC ($|\eta_{\text{det}}| \geq 1.5$). An example of the parametrizations obtained for the second data-taking period is shown in Fig. 3. Systematic uncertainties associated with the method are evaluated by varying the jet sample selection. The difference between the efficiencies derived in different samples is added in quadrature to the statistical uncertainty of the fits.

D. Monte Carlo simulation

We use Monte Carlo simulated samples to calculate selection efficiencies and to simulate kinematic characteristics of the events. Top quark signal and W + jets and Z + jets background processes are generated at $\sqrt{s} = 1.96$ TeV using ALPGEN 1.3.3 [20] for the appropriate matrix element simulation and PYTHIA 6.202 [21] for modeling the initial and final-state radiation, decays, and hadronization. The "tune A" [23] parameter set is used for simulating the underlying event and CTEQ5L [22] for modeling the parton distribution inside the proton and antiproton. Minimum bias simulated proton-antiproton events are superposed on all simulated events after hadronization.

In the $t\bar{t}$ signal simulation we set the top quark mass to 175 GeV and choose the factorization scale for calculation of the $t\bar{t}$ process to be $Q^2 = m_t^2$. We use EVTGEN [24] to provide the branching fractions and lifetimes for all b and c hadrons. The main background consists of W + jets and is

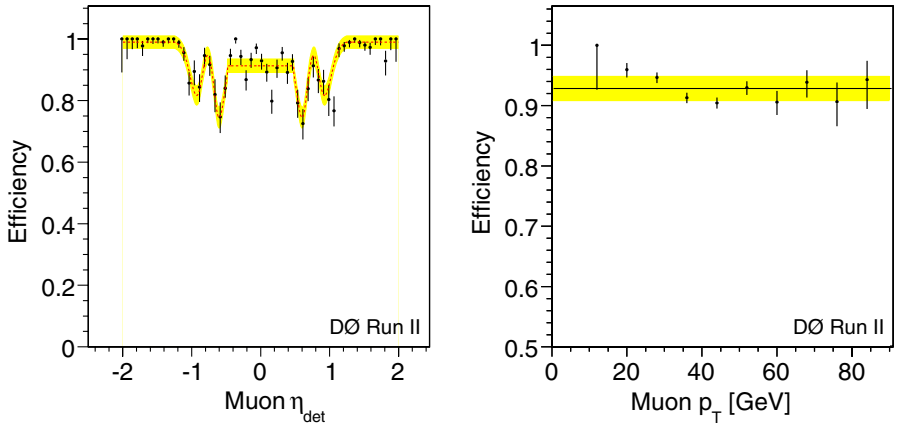

FIG. 2 (color online). Muon trigger efficiencies for the first and second data-taking periods. The parametrization as a function of the muon η_{det} is shown in the upper plot as the dashed line, the statistical error of the fit added in quadrature with the systematic uncertainty is given by the band. The lower plot shows the muon trigger efficiency as a function of the muon p_T and the chosen central value along with the uncertainty band.

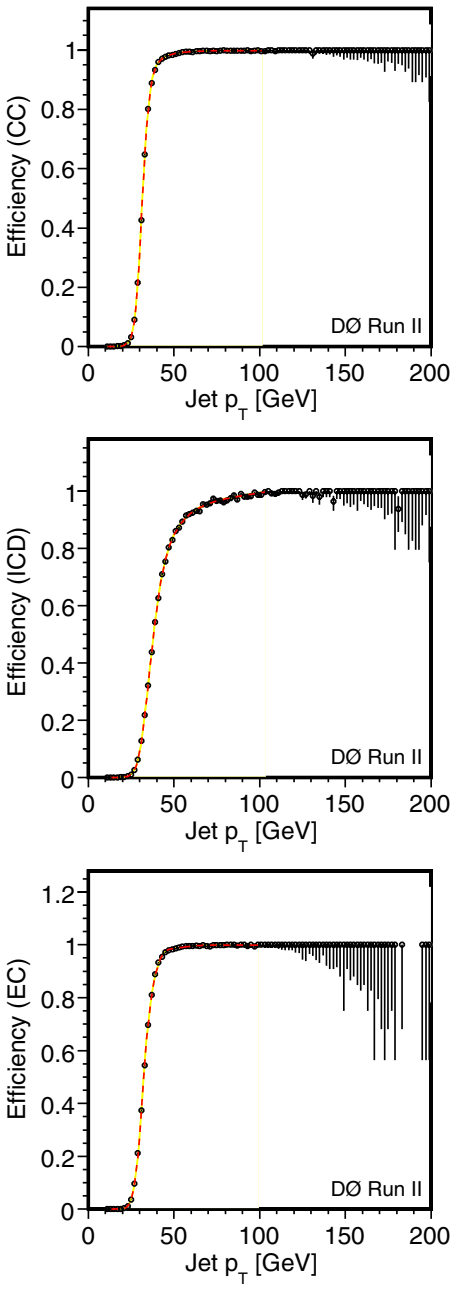

FIG. 3 (color online). The trigger efficiency for a jet to pass L1, L2, and L3 trigger requirements for the three different calorimeter regions: CC (top), ICD (middle), and EC (bottom).

simulated at the factorization scale $M_W^2 + \sum p_{T_j}^2$ where M_W is the W boson mass and p_{T_j} is the transverse momentum of the jet j in the event. For Z + jets events the scale is set to the squared invariant mass of the lepton pair $M_{\ell\ell}^2$. We include virtual photon process (Drell-Yan production) and the interference between the photon and Z boson in the model.

Generated events are processed through the GEANT-based [25] simulation of the D0 detector and are reconstructed with the same program as used for collider data.

E. Calibration of Monte Carlo simulations

We smear (i.e., convolute with a Gaussian) the reconstructed energies of electrons and transverse momenta of muons and jets in the simulation to improve the agreement with the observed momentum resolutions in data, as already described in Secs. III B, III C, and III D. In addition, we correct the simulation for possible inaccuracies in describing individual object identification efficiencies. We derive correction factors to account for the difference in the following efficiencies between data and the simulation: (i) electron (muon) reconstruction and identification, (ii) electron (muon) track match, (iii) electron likelihood, (iv) muon isolation, (v) muon track quality and the distance of closest approach significance (requirements iii and iv of Sec. III C, respectively), (vi) primary vertex selection, and (vii) electron (muon) promptness by comparing the efficiencies measured in $Z \to \ell^+\ell^-$ data events to the ones obtained from the simulation. Two typical examples of the methods used to determine correction factors and their systematic uncertainties are provided below.

To measure the efficiency of electron (muon) reconstruction, we use the same tag and probe method as that used in the trigger efficiency calculation. To avoid bias due

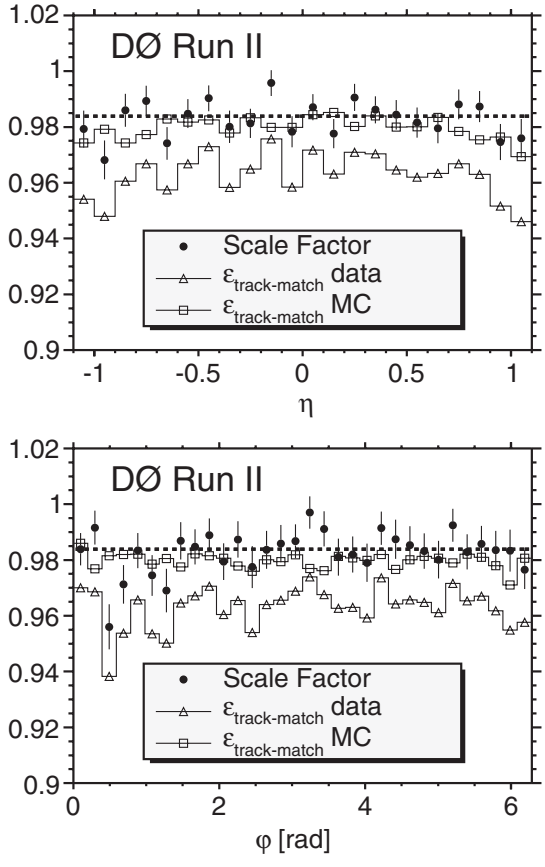

FIG. 4. Track match efficiency in $Z \to e^+e^-$ data and Monte Carlo and their ratio as a function of η (top) and φ (bottom) in CC.

to trigger requirements events used for the measurement have to be recorded with a single electron (muon) trigger, and we require a tag electron (muon) be matched to the electron (muon) trigger object at all trigger levels. We repeat the same measurement using simulated $Z \to \ell^+\ell^-$ events and plot the ratios of the efficiencies as a function of detector η, ϕ, and p_T for muons and, additionally, as a function of the distance to the closest jet in the event for electrons to probe the dependence of the electron reconstruction on the jet activity. Since no strong dependence on any of these quantities is found, we use inclusive factors to correct simulation to data yielding $0.98 \pm 0.027(\text{syst})$ $(1.00 \pm 0.04(\text{syst}))$ for the electron (muon) reconstruction and identification efficiency. Systematic uncertainties are assigned based on the spread of measured ratios in the $\Delta\mathcal{R}(e, \text{jet})$ distribution for electrons and $|\eta_{\text{det}}|$ for muons.

We determine the efficiency of finding a track matched to a electron (muon) by applying the same tag and probe method to $Z \to \ell^+\ell^-$ events selected with a tight electron (muon) as a tag and an electromagnetic cluster satisfying criteria (i)–(iii) of Sec. III B (a muon identified in the muon chambers) as probe for electrons (muons). The correction factors obtained by comparing efficiencies in data and the simulation are found to be $0.983 \pm 0.007(\text{syst})$ for electrons and $0.99 \pm 0.03(\text{syst})$ for muons. Systematic uncertainties arise mainly from the minor dependence of the correction factors on the p_T, η, and ϕ of the leptons. An example of such a dependence is shown in Fig. 4 for the electron track match efficiency.

V. METHOD OVERVIEW

The analysis strategy is outlined briefly in the following. First, we select events that have the same signature as $t\bar{t}$ signal events decaying in the lepton + jets channel, i.e., a truly isolated lepton and genuine $\not\!\!E_T$ from the W boson decay. Multijet events produced by strong interactions are expected to contain neither isolated leptons nor $\not\!\!E_T$. However, they are present in the selected samples due to the imperfect reconstruction in the detector. In particular, the selected e + jets sample contains contributions from multijet events in which a jet is misidentified as an electron. Events where a muon originating from the semileptonic decay of a heavy quark appears isolated contribute to the selected sample in the μ + jets channel. Significant $\not\!\!E_T$ can arise from fluctuations and mismeasurements of the muon and jet energies. In order to model these effects, we use a dedicated data sample to describe the kinematic properties of the surviving multijet events.

The background within the selected samples is dominated by W + jets events. Its contribution is estimated using Monte Carlo simulations. We validate the background model by comparing observed distributions to the predictions from our model in samples of events with low jet multiplicities where only a small signal fraction is expected. For these comparisons we assume a $t\bar{t}$ production cross section of 7 pb as predicted in the SM for a top quark mass of 175 GeV. The Kolmogorov-Smirnov probability for data and simulation to originate from the same underlying distribution is used as an estimator of the quality of the background model and generally good agreement is found.

To extract the fraction of $t\bar{t}$ events in the samples, we select kinematic variables which discriminate between the W + jets background and the $t\bar{t}$ signal, and combine them into a discriminant function. The selected variables are required to be well described by the background model.

In a final step, we derive the discriminant function for the observed data, the $t\bar{t}$ signal, and the electroweak and multijet backgrounds. A Poisson maximum-likelihood fit of the signal and background discriminant distributions to that of the data yields the fraction of $t\bar{t}$ signal and the electroweak and QCD multijet backgrounds in the data sample. Finally, the $t\bar{t}$ production cross section is computed from the number of fitted $t\bar{t}$ events.

In contrast to the $t\bar{t}$ cross section measurement presented in Ref. [26], we do not take advantage of the fact that two jets are expected to contain displaced vertices due to the b-quark decays for signal events. Our cross section estimation is based solely on the different kinematic properties of the signal and background events.

VI. EVENT SELECTION

In both channels, we select events containing one lepton with $p_T > 20$ GeV that passes the tight identification criteria, originates from the primary vertex ($|\Delta z(\ell, \text{PV})| < 1$ cm), and is matched to trigger objects at all relevant levels. We accept muons with $|\eta_{\text{det}}| < 2.0$ and electrons with $|\eta_{\text{det}}| < 1.1$. This choice of cuts is motivated by the acceptance of the D0 muon system and central calorimeter, respectively. Jets in the event are required to have $|\eta| < 2.5$ and $p_T > 20$ GeV except for the highest p_T jet which has to fulfill $p_T > 40$ GeV. Events with a second isolated high transverse momentum lepton are studied elsewhere [27] and explicitly vetoed in the event selection to retain orthogonality between analyses.

In both channels we require $\not\!\!E_T > 20$ GeV to reject multijet backgrounds. However, a significant fraction of multijet events survive this cut due to the presence of heavy flavor decays or jet energy mismeasurement. These events typically have $\not\!\!E_T$ either in the direction of the lepton or back to back to it. Figure 5 illustrates the difference in the angular distribution of $\not\!\!E_T$ and the lepton ($\Delta\varphi(\ell, \not\!\!E_T)$) between signal and multijet background events which we exploit to further suppress the latter.

We performed a grid search in the ($\not\!\!E_T$, $\Delta\varphi(\ell, \not\!\!E_T)$) plane to find cuts that provide the highest product of efficiency and purity for $t\bar{t}$ events, where purity is defined as the ratio of the number of signal $t\bar{t}$ events to the total number of events in the selected sample. The optimal cuts are found

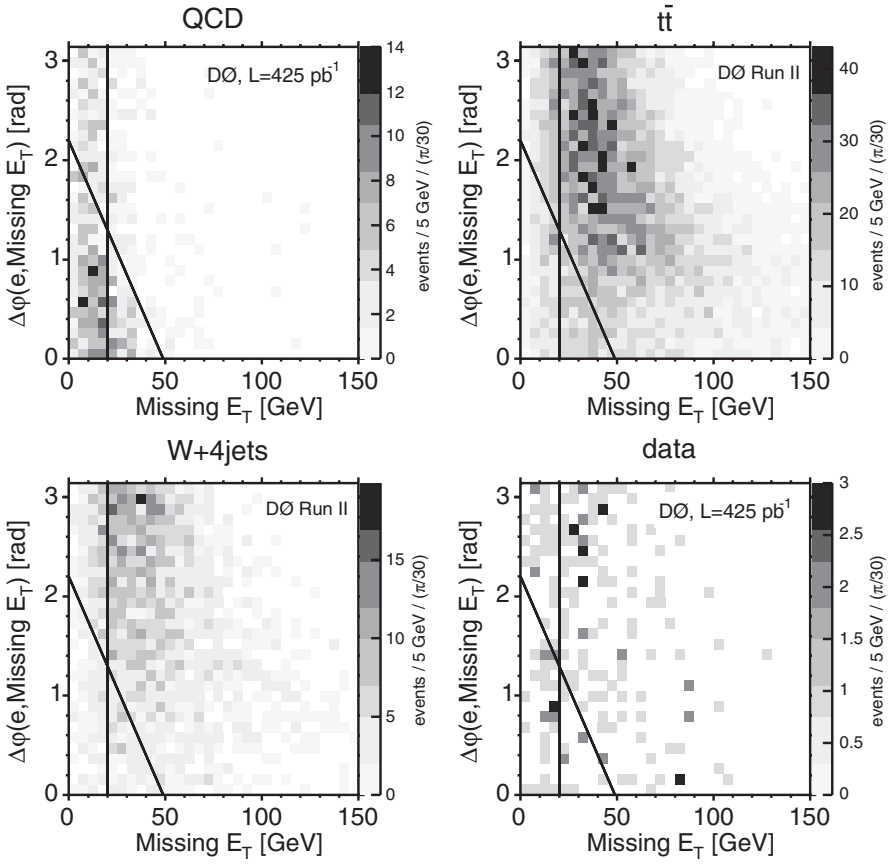

FIG. 5. $\Delta\varphi(e, \not\!\!E_T)$ versus $\not\!\!E_T$ in the multijet QCD data sample, $t\bar{t}$ Monte Carlo, W + jets Monte Carlo, and in data. The lines represent the cuts optimized for the fourth inclusive jet multiplicity bin.

to be $\Delta\varphi(e, \not\!\!E_T) > 0.7\pi - 0.045\not\!\!E_T$ and $\Delta\varphi(\mu, \not\!\!E_T) > 0.6\pi(1 - \not\!\!E_T/(50\,\text{GeV}))$ in e + jets and μ + jets channels, respectively, in addition to the common $\not\!\!E_T > 20$ GeV cut.

The μ + jets channel suffers from a significant contribution of $Z(\mu\mu)$ + jets events which pass the selection criteria due to poor $\not\!\!E_T$ resolution in events with four or more jets. A cut on the invariant di-muon mass of the selected isolated high p_T muon and the additional highest p_T muon with relaxed quality requirements is applied at $70\ \text{GeV} < M_{\mu\mu} < 110$ GeV and rejects roughly 27% of the $Z \rightarrow \mu\mu$ + jet background while keeping almost 100% of the signal in the selected sample. The remaining $Z \rightarrow \mu\mu$ + jets background cannot be rejected since no second muon is reconstructed mainly for reasons of finite acceptance.

The $t\bar{t}$ event selection efficiency is measured using simulated events with respect to all $t\bar{t}$ final states that contain an electron or a muon originating either directly from a W boson or indirectly from the $W \rightarrow \tau\nu$ decay. The branching fractions of such final states are 17.106% and 17.036% [17] for the e + jets and μ + jets channels, respectively. After applying the correction factors discussed in Sec. IV E and the trigger efficiency parametrizations (Sec. IV B) to the simulated $t\bar{t}$ events, the final $t\bar{t}$ selection efficiencies yield $(9.17 \pm 0.09)\%$ and $(9.18 \pm 0.10)\%$ in the e + jets and μ + jets channel, respectively. The quoted uncertainties are statistical only.

VII. BACKGROUNDS

A. Multijet background evaluation

The background within the selected samples is dominated by W + jets events, which have the same final-state signature as $t\bar{t}$ signal events. However, the samples also include contributions from multijet events in which a jet is misidentified as an electron (e + jets channel) or in which a muon originating from the semileptonic decay of a heavy quark appears isolated (μ + jets channel). Significant $\not\!\!E_T$ can arise from fluctuations and mismeasurements of the jet energies and the muon momentum in addition to neutrinos originating from semimuonic heavy quark decays. These instrumental backgrounds are collectively called ''multijet backgrounds,'' and their contribution is estimated directly from data since Monte Carlo simulations do not describe them reliably.

In order to estimate the contribution of the multijet background to the selected data samples we define two samples of events in each channel, a loose and a tight set where the latter is a subset of the former. The loose set (containing N_ℓ events) corresponds to the selected sample

described in the previous paragraph, but with only the loose lepton requirement applied. The tight sample (containing N_t events) additionally demands the selected lepton to pass the tight criteria and is identical to the selected sample. The loose sample consists of N^s events with a truly isolated lepton originating from W + jets, Z + jets, or $t\bar{t}$ events and N^b multijet background events with a fake isolated lepton: $N_\ell = N^s + N^b$. The tight sample consists of $\varepsilon_s N^s$ $t\bar{t}$ signal and electroweak background events and $\varepsilon_b N^b$ multijet background events, where ε_s and ε_b are the efficiencies for a loose lepton to also fulfill the tight lepton requirements.

Solving the system of linear equations for N^b and N^s yields:

$$N^s = \frac{N_t - \varepsilon_b N_\ell}{\varepsilon_s - \varepsilon_b} \quad \text{and} \quad N^b = \frac{\varepsilon_s N_\ell - N_t}{\varepsilon_s - \varepsilon_b}, \qquad (3)$$

and allows the determination of the size of the multijet background contribution in the selected sample. As for the *shape* of the multijet background, for a given variable it is predicted using a data sample where the full selection has been applied except for the tight lepton requirement. Instead, the requirements on the muon isolation in the μ + jets channel and electron likelihood in the e + jets channel are inverted, selecting a data sample enriched in events originating from multijet production processes (''loose-tight'' data sample). However, truly isolated leptons from $t\bar{t}$ and W/Z + jets events will leak into this sample. The composition of the ''loose-tight'' ($N_{\ell-t} = N_\ell - N_t$) data sample can be derived from Eq. (3):

$$N_{\ell-t} = \frac{1-\varepsilon_s}{\varepsilon_s} N_t^s + N_{\ell-t}^b, \qquad (4)$$

where $N_t^s = \varepsilon_s N^s$ is the number of preselected $t\bar{t}$ and electroweak background events as estimated in the following section and $N_{\ell-t}^b$ is the pure multijet contribution to the ''loose-tight'' preselected sample. Using Eq. (4), the contaminations from $t\bar{t}$ and electroweak backgrounds are subtracted bin by bin from the distribution of the ''loose-tight'' preselected data sample in order to predict the shape of the pure multijet contribution for each individual discriminant input variable under consideration.

1. ε_b determination

The rate ε_b at which a lepton in multijet events appears isolated is measured in a data sample which passes the same requirements as the selected one but without applying the $\not\!\!E_T$-related set of cuts discussed in Sec. VI. In this data sample, we calculate ε_b, the ratio of the number of tight events to the number of loose events, as a function of $\not\!\!E_T$. We find that it is constant for $\not\!\!E_T < 10$ GeV, shown in Fig. 6 (top left) for the μ + jets channel, as expected for a sample dominated by the multijet events. The value of ε_b given by the constant fit to data in the $\not\!\!E_T < 10$ GeV region is used in the analysis.

In the muon channel, ε_b does not show significant dependence on the jet multiplicity and does not change between different data-taking periods. However, rather strong dependences are observed with respect to the muon η_{det} (Fig. 6 top right) and transverse momentum (Fig. 6 bottom). We estimated the effect of these dependences on the inclusive ε_b by folding them in with the muon η_{det} and p_T spectra of the selected sample. Since the small number of events with four or more reconstructed jets in the low $\not\!\!E_T$ sample does not allow for a precise measurement we determine ε_b from the events with three or more jets and assign systematic uncertainty from the difference between the flat and the muon p_T-folded measurement:

$$\varepsilon_b = 17.8 \pm 2.0(\text{stat}) \pm 3.1(\text{syst})\%. \qquad (5)$$

In the electron channel we find no significant dependence of ε_b on the jet multiplicity and electron η_{det} and p_T. However, we observe a statistically significant variation of ε_b between different data-taking periods. In particular, we find a higher value of ε_b for events collected during the second data-taking period than during the first one. We attribute this increase to the more stringent electron shower-shape requirements applied at trigger level 3, which improves the quality of the fake electrons that enter our loose sample, making them more likely to pass the tight criterion. Figure 7 shows the electron isolation efficiency as a function of $\not\!\!E_T$ for events with two or more jets, obtained separately for data collected during three data-

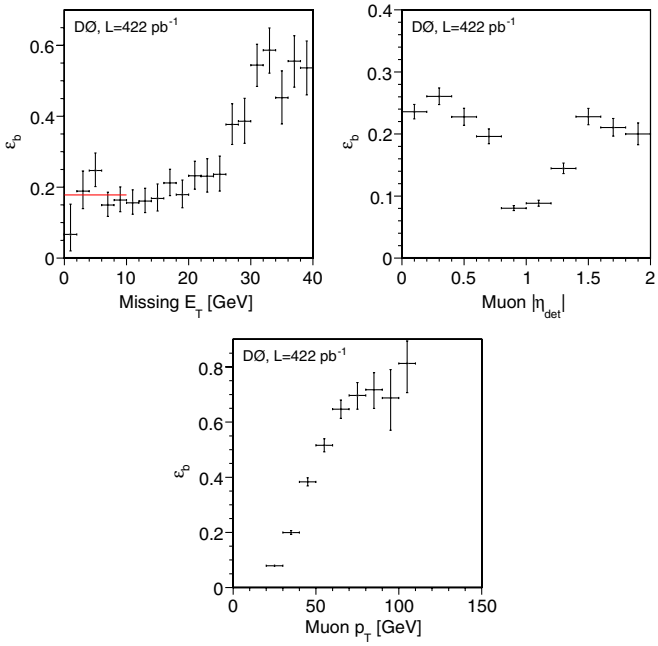

FIG. 6 (color online). Tight muon isolation efficiency ε_b measured in the QCD multijet background dominated data sample as a function of $\not\!\!E_T$ (top left), the muon η_{det} (top right), and p_T (bottom) in μ + jets channel.

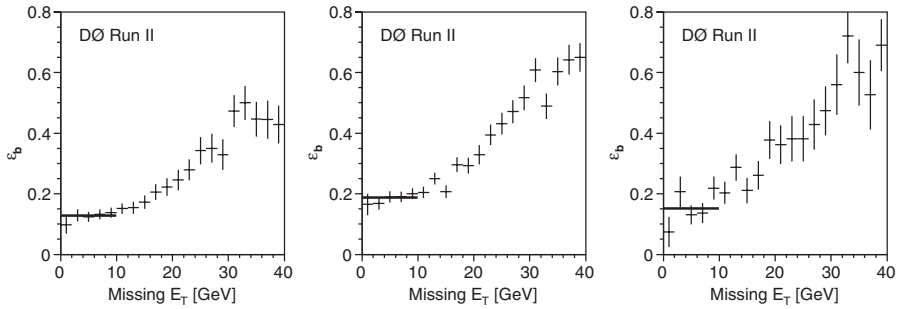

FIG. 7. Electron likelihood efficiency in the QCD multijet background dominated data sample as a function of $\not\!\!E_T$ for events with two or more jets, for the first (left), second (middle), and third (right) data-taking periods. The constant fit to the region of $\not\!\!E_T < 10$ GeV is used to determine the value of ε_b used in the analysis.

taking periods. A fit to these distributions in the region of $\not\!\!E_T < 10$ GeV yields corresponding ε_b. In Eq. (4) we use a luminosity-weighted average ε_b obtained by analyzing events with two or more jets:

$$\varepsilon_b = 16.0 \pm 1.2(\text{stat}) \pm 8.0(\text{syst})\%. \quad (6)$$

The systematic uncertainty of ε_b arises from the small observed variation as a function of jet multiplicity and electron p_T.

2. ε_s determination

The probability ε_s that a truly isolated lepton (i.e., a lepton originating from W boson decays) from a loose sample will survive the tight isolation requirements is measured using simulated W + jets events with four or more jets and corrected with the simulation-to-data scale factor independent of jet multiplicity.

In the muon channel, ε_s depends on the muon p_T spectrum, shown in Fig. 8, and hence is slightly different for W + jets and $t\bar{t}$ events. In the signal jet multiplicity bin ($N_{\text{jet}} \geq 4$), we add the fraction of $t\bar{t}$ events corresponding to the expected $t\bar{t}$ cross section of 7 pb and obtain

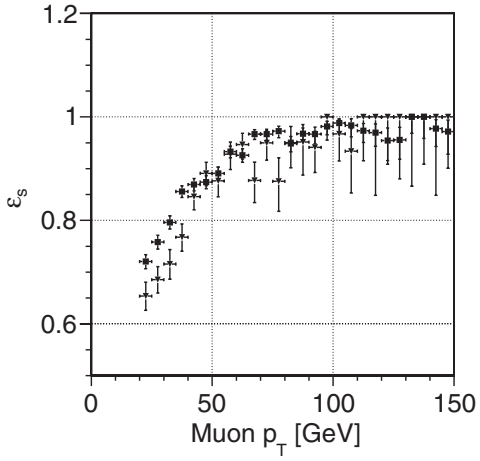

FIG. 8. ε_s as a function of muon p_T for simulated W + jets (triangles) and $t\bar{t}$ (squares) events.

$$\varepsilon_s = 81.8 \pm 0.7(\text{stat})^{+3.3}_{-2.2}(\text{syst})\%, \quad (7)$$

where the systematic uncertainty is derived by varying the $t\bar{t}$ fraction between 0 and 100%. In the electron channel, ε_s determined from the simulated $t\bar{t}$ events agrees with the one obtained from $W+ \geq 4$jets events and yields

$$\varepsilon_s = 82.0 \pm 0.7(\text{stat}) \pm 1.3(\text{syst})\%. \quad (8)$$

Systematic uncertainty arises from the uncertainty on the simulation-to-data correction factor.

B. Expected sample composition

Equation (3) is applied separately to events selected in bins of jet multiplicity for both the e + jets and μ + jets channels. The yields of multijet events N_t^b and events with a real isolated lepton N_t^s in the selected sample with four or more jets are summarized in Table II. Several physics processes contribute to signal-like events N_t^s in the selected sample: $t\bar{t}$ pair production decaying into the ℓ + jets final state, $t\bar{t}$ pair production decaying into two leptons and jets, $t\bar{t} \to \ell\ell' \nu_\ell \nu_{\ell'} b\bar{b}$, where both W bosons decay leptonically, and electroweak background with contributions both from W + jets and Z + jets events.

We estimate the amount of Z + jets background relative to the W + jets background using the cross sections, branching fractions, and selection efficiencies determined using simulated events for both processes:

$$N_{Z+\text{jets}} = \frac{\sigma_{Z+\text{jets}} \cdot \mathcal{B}_{Z\to\mu\mu}}{\sigma_{W+\text{jets}} \cdot \mathcal{B}_{W\to\mu\nu}} \times \frac{\varepsilon_{Z+\text{jets}}}{\varepsilon_{W+\text{jets}}} \times N_{W+\text{jets}}.$$

In the μ + jets channel, the ratio of the Z + jets contribution to the total electroweak background in the selected

TABLE II. Selected sample composition determined using Eq. (3). Only the statistical uncertainties are quoted where appropriate.

Channel	ε_s (%)	ε_b (%)	N_ℓ	N_t	N_t^b	N_t^s
μ + jets	81.8 ± 0.7	17.8 ± 2.0	160	100	8.6 ± 2.0	91.4 ± 10.7
e + jets	82.0 ± 0.7	16.0 ± 1.2	242	119	19.2 ± 2.3	99.8 ± 11.6

sample is measured to be 7%. In the e + jets channel, the Z + jets background is negligible.

The expected contribution from the $t\bar{t}$ dilepton channel is evaluated assuming a standard model cross section of 7 pb for $t\bar{t}$ pair production. The fully corrected efficiencies to select $t\bar{t}$ dilepton events are found to be 0.6% and 0.5% in the e + jets and μ + jets channel, respectively. This results in a 2.0% (2.3%) contribution of dilepton events into the μ + jets (e + jets) final state.

VIII. KINEMATICAL ANALYSIS

The background within the selected samples is dominated by W + jets events, which have the same final state as $t\bar{t}$ signal events. To extract the fraction of $t\bar{t}$ events in the sample we construct a discriminant function that exploits the differences between the kinematic properties of the two classes of events: $t\bar{t}$ signal and W + jets background. All other backgrounds are small and do not justify the introduction of an additional event class.

A. Discriminant function

The discriminant function is built using the method described in Ref. [28], and has the following general form:

$$\mathcal{D} = \frac{S(x_1, x_2, \ldots)}{S(x_1, x_2, \ldots) + B(x_1, x_2, \ldots)}, \tag{9}$$

where $x_1, x_2, \ldots$ is a set of input variables and $S(x_1, x_2, \ldots)$ and $B(x_1, x_2, \ldots)$ are the probability density functions (pdf) for observing a particular set of values $(x_1, x_2, \ldots, x_N)$ assuming that the event belongs to the signal or background, respectively. Neglecting correlations between the input variables, the discriminant function can be approximated by

$$\mathcal{D} = \frac{\prod_i s_i(x_i)/b_i(x_i)}{\prod_i s_i(x_i)/b_i(x_i) + 1}, \tag{10}$$

where $s_i(x_i)$ and $b_i(x_i)$ are the normalized pdfs of each individual variable i for $t\bar{t}$ signal and W + jets background, respectively. In the analysis, we express the discriminant as

$$\mathcal{D} = \frac{\exp(\sum_i (\ln\frac{s_i(x_i)}{b_i(x_i)}))}{\exp(\sum_i (\ln\frac{s_i(x_i)}{b_i(x_i)})) + 1} = \frac{\exp(\sum_i (\ln\frac{s(x_i)}{b(x_i)})^i_{\text{fitted}})}{\exp(\sum_i (\ln\frac{s(x_i)}{b(x_i)})^i_{\text{fitted}}) + 1}, \tag{11}$$

where $(\ln\frac{s}{b})^i_{\text{fitted}}$ is a fit to the logarithm of the ratio of the signal and background pdfs for each kinematic variable i. The application of a fit to the logarithm of the signal to background pdf ratios reduces the influence of individual events on the discriminant output.

B. Selection of discriminating variables

All possible observables with different pdfs for W + jets and $t\bar{t}$ events have the ability to discriminate between the two. As a first step toward the goal of selecting an optimal set of discriminating input variables, we first evaluate the separation power for a large set of individual variables by estimating the expected total uncertainty of the $t\bar{t}$ cross section when using the variable under consideration as sole discriminator. Variables are then ranked and selected by increasing uncertainty. The total expected uncertainty is estimated by adding the systematic uncertainties related to jet energy scale (JES), jet energy resolution (JER), and jet reconstruction efficiency (JID) in quadrature to the statistical uncertainty:

$$\sigma_{\text{tot}} = \sqrt{\left(\frac{\sigma_{\text{stat}}}{\sqrt{2}}\right)^2 + \sigma^2_{\text{JES}} + \sigma^2_{\text{JER}} + \sigma^2_{\text{JID}}}. \tag{12}$$

The optimization is done in e + jets and μ + jets channels separately. Therefore the statistical uncertainty in Eq. (12) is reduced by a factor of $1/\sqrt{2}$, since the additional data from the complementary channel roughly doubles the statistics in the combination. We select a set of 13 variables described in the appendix as input for the second step of the discriminant function optimization.

C. Optimization of the discriminant function

The optimization procedure, determining which combination of topological input variables will form the final discriminant function, is performed by estimating the expected combined statistical and systematic uncertainty of the measured $t\bar{t}$ cross section. The expected uncertainty is calculated for all discrimination functions that can be constructed from the selected input variables by using all possible subsets of the 13 variables in turn as input. Pseudoexperiments are performed by drawing pseudodata discriminant output distributions from the output discriminant distributions of simulated events. The composition of such a pseudodataset is taken according to the expected sample composition for $N_{\text{jet}} \geq 4$ and $\sigma_{t\bar{t}} = 7$ pb and allowing Poisson fluctuations. Three thousand pseudoexperiments are built for each source of statistical or systematic uncertainty and the discriminant function under consideration. We select the discriminant function which provides the smallest expected total uncertainty, including all sources of systematic uncertainties that affect the shape of the discriminant function.

In the μ + jets channel the discriminant constructed with the following five input variables shows the best performance: (i) H_T, the scalar sum of the p_T of the four leading jets; (ii) $\sum \eta^2$, the sum of the squared pseudorapidities of the four leading jets; (iii) M_T, transverse mass of the four leading jets; (iv) the event centrality $\mathcal{C}$, defined as the ratio of the scalar sum of the p_T of the jets to the scalar sum of the energy of the jets; (v) the event aplanarity $\mathcal{A}$,

constructed from the four-momenta of the lepton and the jets. Aplanarity characterizes the event shape and is defined, for example, in Ref. [29].

In the e + jets channel the optimal discriminant function is found to be built from six variables: (i) NJW, the weighted number of jets in the event; (ii) the event centrality $\mathcal{C}$; (iii) the event aplanarity $\mathcal{A}$; (iv) $|\eta_{\text{jet}}|^{\text{max}}$, $|\eta|$ of the jet with maximum pseudorapidity; (v) minimum of the invariant mass of any two jets in the event; (vi) M_T, transverse mass the four leading jets. The normalized distributions of the selected kinematic variables for $t\bar{t}$ signal and the W + jets background are shown in Figs. 9 and 10 for μ + jets and e + jets channels, respectively. A more detailed explanation of the used variables is given in the appendix. Figure 11 demonstrates that distributions in data of the kinematic variables selected as input to the discriminant are well described by the sum of expected $t\bar{t}$ signal, W + jets, and multijet background contributions for events with three jets dominated by the background.

The discriminant function is built according to Eq. (11), from the fits to the logarithm of the ratio of signal ($t\bar{t}$) over background (W + jets) based on simulated events. Finally, the fully defined discriminant function is evaluated for each physics process considered in this analysis. For this purpose, we use simulated $t\bar{t}$ events with ℓ + jets and dilepton final states, W/Z + jets events, and the multijet background data sample selected by requiring that the lepton fails the tight selection criterion. An example of the discriminant distributions for the $t\bar{t}$ signal and main backgrounds in the e + jets channel is shown in Fig. 12. By construction, the discriminant function peaks near zero for the background, and near unity for the signal.

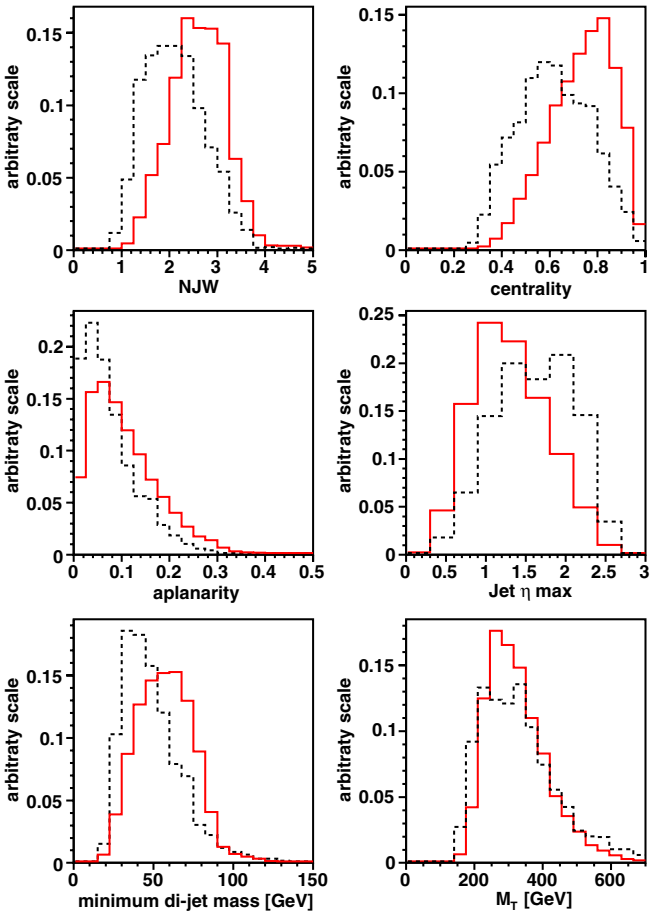

FIG. 10 (color online). Distributions of the six variables used as input to the likelihood discriminant in the e + jets channel. The $t\bar{t}$ signal (solid line) and W + jets background (dashed line) are derived from simulations.

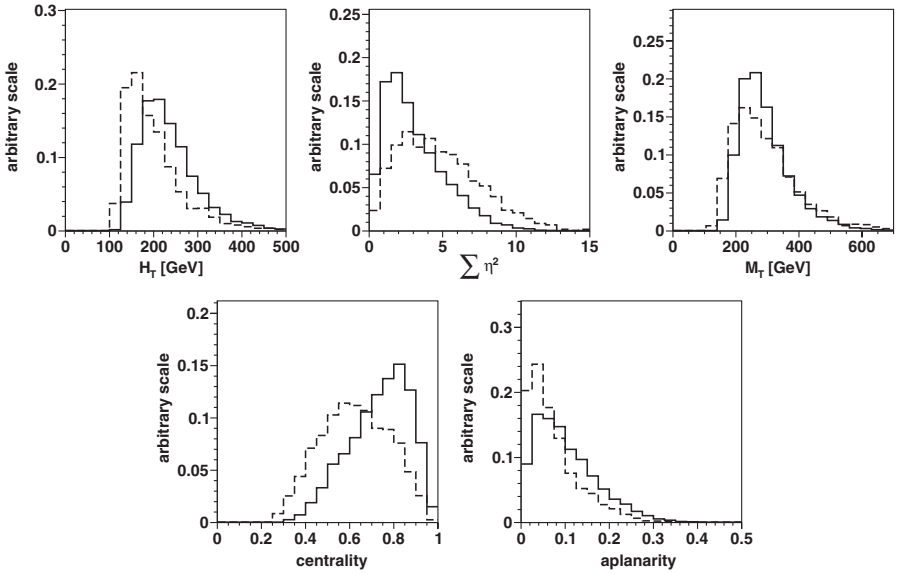

FIG. 9. Distributions of the five variables used as input to the likelihood discriminant in the μ + jets channel. The $t\bar{t}$ signal (solid line) and combined W/Z + jets electroweak backgrounds (dashed line) are derived from simulations.

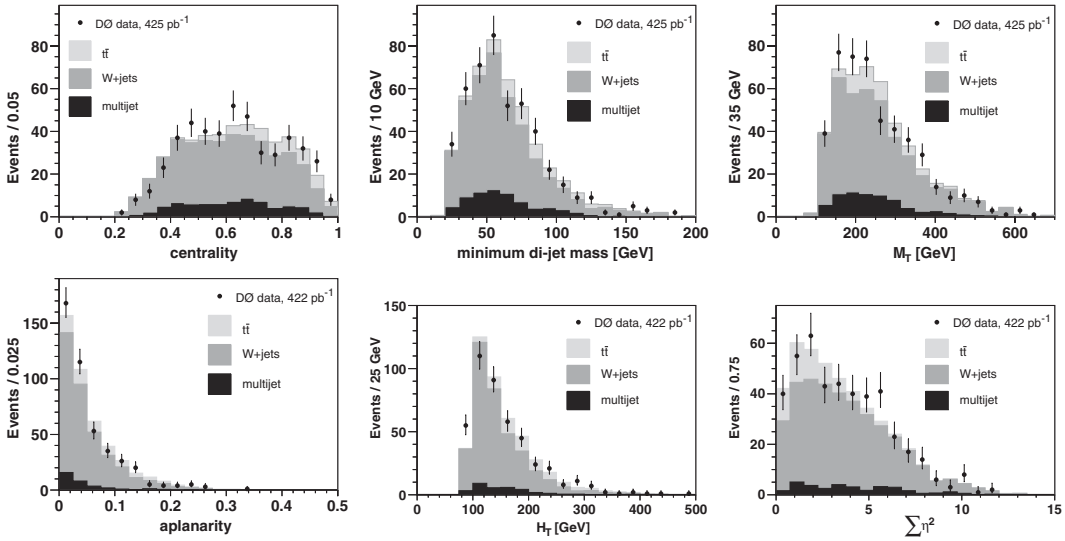

FIG. 11. Distributions of selected variables used as input to the discriminant in data overlaid with the predicted background and expected $t\bar{t}$ signal for the events with exactly three jets in the e + jets (top row) and μ + jets (bottom row) channels.

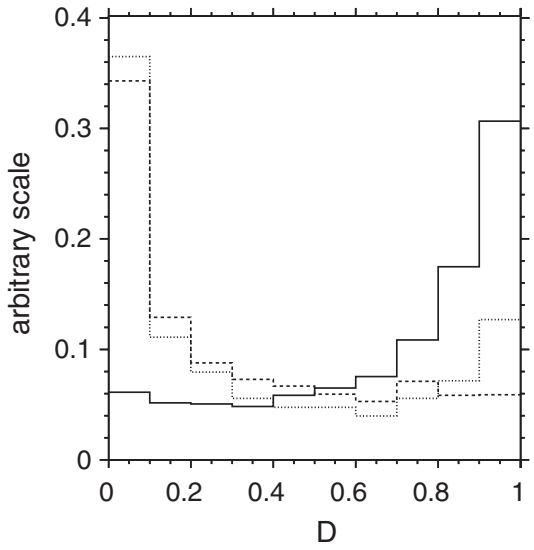

FIG. 12. Discriminant function output distributions for the $t\bar{t}$ signal (solid line), W + jets background (dashed line), and multijet events (dotted line) in the e + jets channel.

IX. CROSS SECTION EXTRACTION

A. Method

The number of $t\bar{t}$ events in the selected data sample is extracted by performing a maximum-likelihood fit to the discriminant distribution observed in data using templates for the $t\bar{t}$ signal, multijet, and W/Z + jets (W + jets) backgrounds in the μ + jets (e + jets) channel. The Z + jets contribution is added to the W + jets discriminant template according to its fraction determined in Sec. VII B, resulting in a combined electroweak background template in the μ + jets channel. Similarly, the contributions from the dilepton and ℓ + jets $t\bar{t}$ signals are combined into a single $t\bar{t}$ template before fitting by adding the dilepton contribution to the ℓ + jets template. Dilepton and Z + jets admixtures introduce only small corrections to the $t\bar{t}$ ℓ + jets and W + jets template shape, respectively.

We consider three different contributions to the maximum-likelihood fit: $t\bar{t}$, W/Z + jets, and multijet, and constrain the relative fraction of the latter using Eq. (3). This is realized by defining the following likelihood function:

$$L(N_t^{t\bar{t}}, N_t^W, N_t^b) = \left[\prod_i \mathcal{P}(n_i^o, \mu_i)\right] \mathcal{P}(N_{\ell-t}^o, N_{\ell-t}), \quad (13)$$

where $\mathcal{P}(n, \mu)$ denotes the Poisson probability density function for n observed events given an expectation value of μ and $N_t^{t\bar{t}}$, N_t^W, N_t^b are the numbers of $t\bar{t}$, W/Z + jets, and multijet events in the selected sample, respectively. In the first term of Eq. (13), i runs over all bins of the discriminant histogram; n_i^o is the content of bin i measured in the selected data sample; and μ_i is the expectation for bin i, which is a function of $N_t^{t\bar{t}}$, N_t^W, and N_t^b as given by

$$\mu_i(N_t^{t\bar{t}}, N_t^W, N_t^b) = f_i^{t\bar{t}} N_t^{t\bar{t}} + f_i^W N_t^W + f_i^b N_t^b, \quad (14)$$

where $f_i^{t\bar{t}}$, f_i^W, f_i^b represent the fractions in bin i of the $t\bar{t}$, W + jets, and multijet discriminant templates (shown in Fig. 12 for e + jets channel), respectively. The second term of Eq. (13) effectively implements the constraint on N_t^b via the Poisson probability of the observed number of events in the "loose-tight" ($N_{\ell-t}^o$) sample, given the expectation ($N_{\ell-t}$). The latter can be expressed as

$$N_{\ell-t} = \frac{1-\varepsilon_s}{\varepsilon_s} N_t^{t\bar{t}} + \frac{1-\varepsilon_s}{\varepsilon_s} N_t^W + \frac{1-\varepsilon_b}{\varepsilon_b} N_t^b. \quad (15)$$

Thus, the task is to minimize the negative log-likelihood function

TABLE III. Fitted number of $t\bar{t}$, W + jets, and multijet background events in the selected sample in the e + jets and μ + jets channels. N_t^W includes the Z + jets contribution in the μ + jets sample.

Channel	$N_t^{t\bar{t}}$	N_t^W	N_t^b
e + jets	$67.5^{+13.8}_{-12.9}$	$32.6^{+14.0}_{-13.0}$	19.3 ± 2.0
μ + jets	$21.1^{+10.7}_{-9.7}$	$72.6^{+13.0}_{-12.1}$	$8.1^{+1.8}_{-1.7}$

$$-\log L(N_t^{t\bar{t}}, N_t^W, N_t^b) \simeq \sum_i (-n_i^o \log \mu_i + \mu_i) - N_{\ell-t}^o \log N_{\ell-t} + N_{\ell-t},$$

where any terms independent of the minimization parameters are dropped. The fitted parameters $(N_t^{t\bar{t}}, N_t^W, N_t^b)$ are given by their value at the negative log-likelihood function minimum, and their uncertainties are obtained by raising the negative log likelihood by one half unit above the minimum while all other parameters of the fit are allowed to float. The results of the fits are listed in Table III and the corresponding correlation coefficients are summarized in Table IV.

One complication arises due to the fact that the shape of the discriminant for the multijet background is obtained from the ''loose-tight'' data sample which has a small contribution from W + jets and $t\bar{t}$ events (Eq. (15)). The contamination of the multijet template is taken into account by using the corrected expected number of events in each bin of the discriminant function

$$\mu_i(N_t^{t\bar{t}}, N_t^W, N_t^b) = (f_i^{t\bar{t}} N_t^{t\bar{t}} + f_i^W N_t^W) \times \left(1 - \frac{\varepsilon_b}{1-\varepsilon_b} \times \frac{1-\varepsilon_s}{\varepsilon_s}\right) + f_i^b \left(N_t^b + \frac{\varepsilon_b}{1-\varepsilon_b} \frac{1-\varepsilon_s}{\varepsilon_s} \times (N_t^{t\bar{t}} + N_t^W)\right),$$

in place of the one of Eq. (14).

Figure 13 shows the distributions of the discriminant functions for data in e + jets and μ + jets channels along with the fitted contributions from the $t\bar{t}$ signal and W + jets and multijet backgrounds.

TABLE IV. Matrices of correlation coefficients of the likelihood fit in the e + jets and μ + jets channels.

	e + jets			μ + jets		
	$N_t^{t\bar{t}}$	N_t^W	N_t^b	$N_t^{t\bar{t}}$	N_t^W	N_t^b
$N_t^{t\bar{t}}$	+1.00	−0.63	−0.11	+1.00	−0.59	−0.14
N_t^W		+1.00	−0.23		+1.00	−0.23
N_t^b			+1.00			+1.00

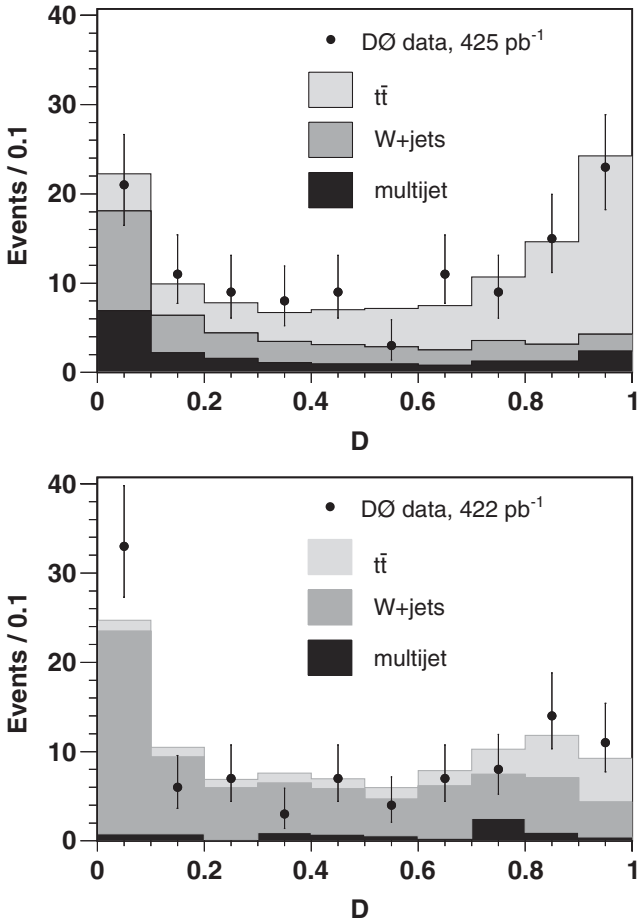

FIG. 13. Discriminant distribution for data overlaid with the result from a fit of $t\bar{t}$ signal, and W + jets and multijet background in the e + jets (upper plot) and μ + jets (lower plot) channel.

B. Cross sections in individual channels

The $t\bar{t}$ production cross section for an individual channel j is computed as

$$\sigma_j = \frac{N_t^{t\bar{t}}(j)}{\varepsilon_j \mathcal{B}_j \mathcal{L}_j}, \tag{16}$$

where $N_t^{t\bar{t}}(j)$ is the number of fitted $t\bar{t}$ events in channel j, $\mathcal{B}_j$ is the branching fraction for the $t\bar{t}$ final state where the lepton is allowed to originate either directly from a W boson or from the $W \to \tau\nu$ decay ($\mathcal{B}_{\text{ljets}}$), $\mathcal{L}_j$ is the integrated luminosity, and ε_j is the $t\bar{t}$ selection efficiency. The efficiencies ε are obtained by correcting the $t\bar{t}$ ℓ + jets selection efficiencies $\varepsilon_{\text{ljets}}$ for the $t\bar{t}$ dilepton final-state contribution:

$$\varepsilon = \varepsilon_{\text{ljets}} + \frac{\mathcal{B}_{\ell\ell}}{\mathcal{B}_{\text{ljets}}} \varepsilon_{\ell\ell}, \tag{17}$$

where $\varepsilon_{\ell\ell}$ and $\mathcal{B}_{\ell\ell}$ are the selection efficiency and the branching fraction for the $t\bar{t} \to \ell\ell$ + jets decay channel.

TABLE V. Number of selected events in the loose (N_ℓ) and tight (N_t) sample, branching fraction ($\mathcal{B}$), integrated luminosity ($\mathcal{L}$), selection efficiency for $t\bar{t} \to \ell$ + jets ($\varepsilon_{\text{ljets}}$), and total selection efficiency (ε) in e + jets and μ + jets channels.

Channel	N_l	N_t	$\mathcal{B}$	$\mathcal{L}$ (pb^{-1})	$\varepsilon_{\text{ljets}}$ (%)	ε (%)
e + jets	242	119	0.171 06	425	9.17	9.39
μ + jets	160	100	0.170 36	422	9.18	9.36

The input values for the likelihood fit are summarized in Table V.

The $t\bar{t}$ production cross sections at $\sqrt{s} = 1.96$ TeV for a top quark mass of 175 GeV in the e + jets and μ + jets channels are measured to be

$$e + \text{jets: } \sigma_{t\bar{t}} = 9.9^{+2.1}_{-1.9}(\text{stat}) \pm 1.0(\text{syst}) \pm 0.6(\text{lum}) \text{ pb};$$

$$\mu + \text{jets: } \sigma_{t\bar{t}} = 3.1^{+1.6}_{-1.5}(\text{stat}) \pm 0.4(\text{syst}) \pm 0.2(\text{lum}) \text{ pb}.$$

C. Combined cross section

The combined cross section in the lepton + jets channel is estimated by minimizing the sum of the negative log-likelihood functions of each individual channel. A total of five parameters are simultaneously fitted: $\sigma_{t\bar{t}}$ (common to both lepton channels) and $N_t^W(j)$ and $N_t^b(j)$ separately for each channel. Figure 14 shows the distribution of the discriminant function for data along with the fitted contributions from $t\bar{t}$ signal, W + jets, and multijet background events which are found to be 40%, 48%, and 12%, respectively. The combined cross section for a top quark mass of 175 GeV is

$$\sigma_{t\bar{t}}(175 \text{ GeV}) = 6.4^{+1.3}_{-1.2}(\text{stat}) \pm 0.7(\text{syst}) \pm 0.4(\text{lum}) \text{ pb}.$$

In the following we estimate the probability to observe the cross sections measured in the e + jets and μ + jets channels under the assumption that they both originate from the same underlying cross section. We consider the combined cross section of 6.4 pb to be our best estimate of the "true" cross section. We generate pseudoexperiments assuming this cross section both in the e + jets and μ + jets channels. The expected statistical and systematic uncertainties are evaluated at this value taking into account correlations between the uncertainties in both channels. We find that the correlation between the two measurements is small, 3.3%, since the dominant uncertainties are of statistical nature and therefore uncorrelated between the channels. The probability to observe the $t\bar{t}$ cross section above 9.9 pb in the e + jets (below 3.1 pb in the μ + jets) channel given the true cross section of 6.4 pb is 4.8% (5.1%).

We estimate the consistency of the observed cross sections in individual channels by analyzing the distribution of the difference between the e + jets and μ + jets cross sections obtained in each pseudoexperiment described above. We find that this distribution can be fitted by a Gaussian centered at zero with a width of 2.87 pb. Thus the probability to measure cross sections in the individual channels that differ by the observed difference of 6.8 pb or more is 1.8%. We conclude that the cross sections in the e + jets and μ + jets channels agree within 2.4 standard deviations, and the difference between the measured cross sections is attributed to a statistical fluctuation.

We have studied the dependence of the measured cross section on the top quark mass by using the samples of simulated $t\bar{t}$ events with different top quark masses to evaluate signal efficiencies and discriminant function outputs and repeating complete analysis. Figure 15 shows the dependence of the combined cross section in the lepton + jets channel on the top quark mass. The solid line represents the fit to the measured cross sections for various masses of the top quark. For 170 GeV $< m_{\text{top}} <$ 180 GeV the cross section changes as a function of m_{top} as

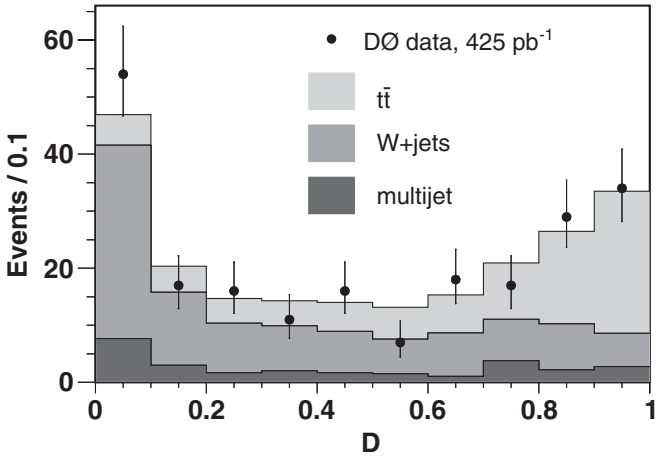

FIG. 14. Discriminant distribution for data overlaid with the result from a fit of $t\bar{t}$ signal, and W + jets and multijet background in the combined ℓ + jets channel.

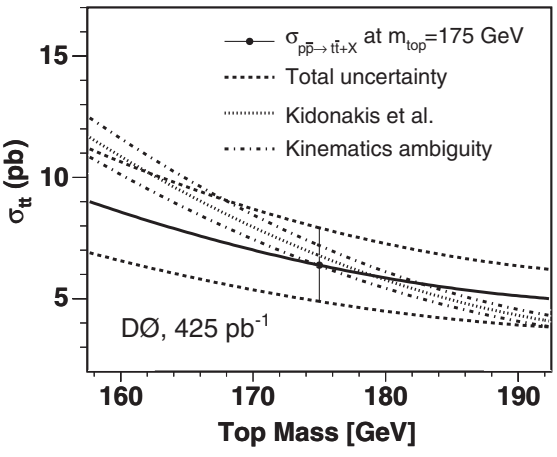

FIG. 15. The combined $t\bar{t}$ production cross section in the lepton + jets channel as a function of top quark mass compared to the theoretical calculations [6].

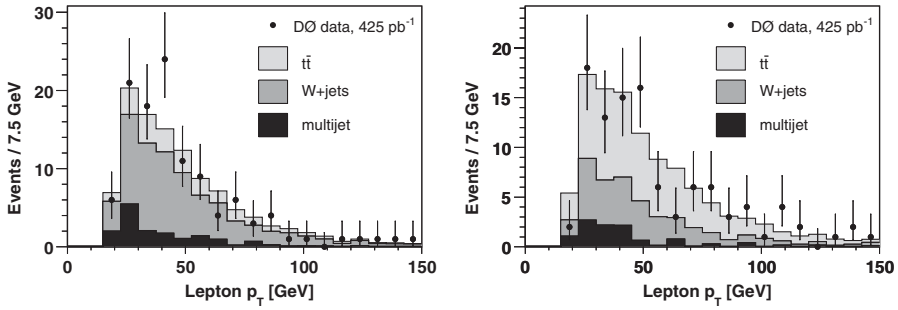

FIG. 16. Lepton p_T distribution for ℓ + jets events in data with discriminant below 0.5 (left plot) and discriminant above 0.5 (right plot), overlaid with the result from a fit of $t\bar{t}$ signal, and W + jets and multijet background.

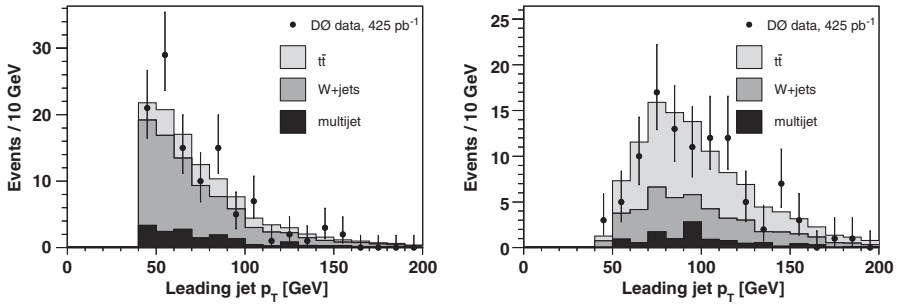

FIG. 17. Leading jet p_T distribution for ℓ + jets events in data with discriminant below 0.5 (left plot) and discriminant above 0.5 (right plot), overlaid with the result from a fit of $t\bar{t}$ signal, and W + jets and multijet background.

$$\sigma_{t\bar{t}}(m_{\rm top}) = \sigma_{t\bar{t}} - 0.1\,\frac{\rm pb}{\rm GeV} \times (m_{\rm top} - 175\ {\rm GeV}). \quad (18)$$

The kinematic distributions observed in lepton + jets events are well described by the sum of $t\bar{t}$ signal, W/Z + jets, and multijet background contributions. An example of this agreement is illustrated in Figs. 16 and 17 for events selected requiring $\mathcal{D} < 0.5$, i.e., dominated by background, and events in the $t\bar{t}$ signal region with $\mathcal{D} > 0.5$. The two variables shown are the lepton p_T and the highest jet p_T in the event and are not used as input to the discriminant function.

X. SYSTEMATIC UNCERTAINTIES

The systematic uncertainty on the $t\bar{t}$ production cross section in an individual channel j for each independent source of systematic uncertainty i is determined by varying the source by 1 standard deviation up and down and propagating the variation into both the fitted number of $t\bar{t}$ events and the signal efficiency resulting in a new value of the cross section in channel j:

$$\sigma_j^i = \sigma_j \pm \Delta\sigma_j^i = \frac{N_t^{t\bar{t}}(j) \pm \Delta N_t^{t\bar{t}}(j)^i}{(\varepsilon_j \pm \Delta\varepsilon_j^i)\mathcal{B}_j\mathcal{L}_j}. \quad (19)$$

Variations due to uncertainty sources which modify simultaneously both the selection efficiency and the fitted number of $t\bar{t}$ events are treated as fully correlated.

The variation of the fitted number of $t\bar{t}$ events due to each individual source i is estimated by generating 10 000 pseudoexperiments from simulated events. The sample composition of each pseudodataset is the same as the measured sample composition in data but allowing for Poisson fluctuations in the number of events from a specific contribution. The discriminant distribution for each pseudodataset is fitted in order to extract $N_{t\bar{t}}$ once with the default discriminant function templates for $t\bar{t}$, W/Z + jets, and multijet background and once with the varied ones. The relative difference between the two results is histogrammed. The relative systematic uncertainty is extracted from the histogram by performing a fit to a Gaussian distribution around the most probable value and using the mean of the fit as an estimator for the relative uncertainty on the fitted number of $t\bar{t}$ events from source i.

Positive (negative) variations of the cross section $\Delta\sigma_j^i$ from each individual source of systematics with respect to the central value σ_j (Eq. (19)) are summed quadratically to obtain total positive (negative) systematic uncertainty. In addition, a systematic uncertainty of $\pm 6.1\%$ from the luminosity measurement is assigned [15]. By construction, this method does not allow the systematic uncertainties to affect the central value of the cross section σ_j.

The systematic uncertainty on the combined cross section is estimated following the same procedure as described above taking into account the correlations between individual sources of systematic uncertainties

TABLE VI. Summary of systematic uncertainties of the cross section $\Delta\sigma_{t\bar{t}}$ (pb).

Source	e + jets	μ + jets	ℓ + jets
Primary vertex	$+0.30 - 0.28$	$+0.12 - 0.10$	$+0.24 - 0.21$
Lepton ID	± 0.32	$+0.17 - 0.16$	± 0.22
Jet energy scale	$+0.70 - 0.72$	$+0.05 - 0.16$	± 0.47
Jet ID	$+0.08 - 0.14$	$+0.11 - 0.02$	$+0.03 - 0.08$
Trigger	$+0.05 - 0.21$	$+0.09 - 0.08$	$+0.10 - 0.20$
W bckg model	$+0.11 - 0.21$	$+0.13 - 0.11$	$+0.12 - 0.18$
Multijet bckg	± 0.04	$+0.13 - 0.14$	$+0.05 - 0.06$
MC statistics	± 0.48	± 0.31	± 0.33
$\mathcal{B}$	$+0.20 - 0.19$	± 0.06	± 0.14
Subtotal	$+0.99 - 1.03$	± 0.44	$+0.70 - 0.72$
Luminosity	± 0.64	± 0.20	± 0.42
Total	$+1.18 - 1.21$	± 0.45	$+0.82 - 0.83$

between the channels. The systematic uncertainties are classified as either uncorrelated (usually of statistical origin in either Monte Carlo simulation or data) or fully correlated between the channels. In particular, we consider the systematic uncertainties coming from the primary vertex reconstruction, jet energy calibration, jet identification, jet trigger, W background model, and branching fraction to be fully correlated. Uncertainties associated with the lepton identification, lepton trigger, multijet background evaluation, and the limited statistics of Monte Carlo samples are taken as uncorrelated in the cross section combination.

Table VI summarizes the contributions from the various sources of systematic uncertainties to the total systematic uncertainty on the cross sections in the e + jets, μ + jets, and combined ℓ + jets channels. The jet energy scale uncertainty dominates, followed by the uncertainty of the luminosity measurement. These two represent 80% of the total systematic uncertainty of the combined cross section.

XI. SUMMARY

We have measured the $t\bar{t}$ production cross section in the ℓ + jets final state by combining the measurements performed in the individual e + jets and μ + jets channels yielding

$$e + \text{jets: } \sigma_{t\bar{t}} = 9.9^{+2.1}_{-1.9}(\text{stat}) \pm 1.0(\text{syst}) \pm 0.6(\text{lum})\text{pb};$$

$$\mu + \text{jets: } \sigma_{t\bar{t}} = 3.1^{+1.6}_{-1.5}(\text{stat}) \pm 0.4(\text{syst}) \pm 0.2(\text{lum})\ \text{pb}.$$

The observed difference in the cross sections at the level of 2.4 standard deviations is attributed to a statistical fluctuation.

The combined cross section for a top quark mass of 175 GeV is

$$\ell + \text{jets: } \sigma_{t\bar{t}} = 6.4^{+1.3}_{-1.2}(\text{stat}) \pm 0.7(\text{syst}) \pm 0.4(\text{lum})\ \text{pb}.$$

The result is in good agreement with the theoretical predictions of $6.7^{+0.7}_{-0.9}$ pb [7] and 6.8 ± 0.6 pb [6] based on the full NLO matrix elements and the resummation of the leading and next-to-leading soft logarithms.

ACKNOWLEDGMENTS

We thank the staffs at Fermilab and collaborating institutions, and acknowledge support from the DOE and NSF (USA); CEA and CNRS/IN2P3 (France); FASI, Rosatom, and RFBR (Russia); CAPES, CNPq, FAPERJ, FAPESP, and FUNDUNESP (Brazil); DAE and DST (India); Colciencias (Colombia); CONACyT (Mexico); KRF and KOSEF (Korea); CONICET and UBACyT (Argentina); FOM (The Netherlands); Science and Technology Facilities Council (United Kingdom); MSMT and GACR (Czech Republic); CRC Program, CFI, NSERC, and WestGrid Project (Canada); BMBF and DFG (Germany); SFI (Ireland); The Swedish Research Council (Sweden); CAS and CNSF (China); Alexander von Humboldt Foundation; and the Marie Curie Program.

APPENDIX: KINEMATIC VARIABLES FOR DISCRIMINANT OPTIMIZATION

We select a set of 13 variables as input for the discriminant function optimization. These variables are designed to address different aspects of the $t\bar{t}$ signal and W + jets background kinematics: event energy, shape, location of the jets in the detector, properties of soft nonleading jets, etc. W + jets background tends to have a lower event transverse energy, less energetic jets, and smaller total invariant mass than $t\bar{t}$ events. Since the $t\bar{t}$ system is produced nearly at rest at the Tevatron and therefore is expected to have a much smaller boost in the beam direction than W + jets, the jets from a $t\bar{t}$ event are more central. The $t\bar{t}$ event topology is also different from W + jets due to the different production mechanisms.

We select the following 13 variables for the discriminant function optimization:

(i) H_T, the scalar sum of the p_T of the four leading jets;
(ii) H_T', H_T divided by the scalar sum of the absolute values of p_z of the jets, the lepton, and the $\not\!\!E_T$;
(iii) M_T, transverse mass of the four leading jets;
(iv) M_{event}, invariant mass of up to four leading jets, the $\not\!\!E_T$, and the lepton in the event;
(v) Event centrality $\mathcal{C}$, defined as the ratio of the scalar sum of the p_T of the jets to the scalar sum of the energy of the jets;
(vi) Event aplanarity $\mathcal{A} = \frac{3}{2}\lambda_3$ and sphericity $\mathcal{S} = \frac{3}{2} \times (\lambda_2 + \lambda_3)$, derived from the normalized momentum tensor, defined by $\mathcal{M}_{ij} = \frac{\Sigma_o p_i^o p_j^o}{\Sigma_o |\vec{p}^o|^2}$, where $\vec{p}^o$ is the momentum vector of jet o, i, and j are Cartesian coordinates, and the eigenvalues λ_k of $\mathcal{M}$ are ordered such that $\lambda_1 \geq \lambda_2 \geq \lambda_3$ with $\lambda_1 + \lambda_2 + \lambda_3 = 1$;
(vii) $\Delta\varphi(\ell, \not\!\!E_T)$, angle between the lepton and the $\not\!\!E_T$ direction perpendicular to the beam axis;
(viii) $|\eta_{\text{jet}}|^{\text{max}}$, $|\eta|$ of the jet with maximum pseudorapidity;
(ix) $\sum \eta^2$, sum of the squared pseudorapidities of up to four jets;

(x) NJW, built from the transverse momenta of up to four leading jets, it corresponds to the jet multiplicity above a given jet p_T threshold, over the range between 10 GeV and 55 GeV, weighted by the threshold, and is sensitive to the additional radiation in the event and to the p_T spectrum of the jets in the event [30];

(xi) M_{inv}^{123}, sum of invariant masses of the three dijet pairs formed from the three leading jets in the event;

(xii) $M_{\text{dijet}}^{\text{min}}$, the minimum of the invariant mass of any two jets in the event.

Variables that characterize the event energy scale (H_T, H_T', M_T, M_{event}) show the best discrimination power, but they are sensitive to the jet energy calibration, which is one of the dominant sources of systematic uncertainty on the $t\bar{t}$ cross section. A combination of variables belonging to different classes provides the best total uncertainty on the cross section.

[1] F. Abe *et al.* (CDF Collaboration), Phys. Rev. Lett. **74**, 2626 (1995); S. Abachi *et al.* (D0 Collaboration), Phys. Rev. Lett. **74**, 2632 (1995).

[2] V. Abazov *et al.* (D0 Collaboration), Phys. Lett. B **622**, 265 (2005); D. Acosta *et al.* (CDF Collaboration), Phys. Rev. D **71**, 012005 (2005).

[3] V. Abazov *et al.* (D0 Collaboration), Phys. Rev. Lett. **98**, 181802 (2007).

[4] T. Affolder *et al.* (CDF Collaboration), Phys. Rev. D **64**, 032002 (2001);V. Abazov *et al.* (D0 Collaboration), Phys. Rev. D **67**, 012004 (2003).

[5] R. Bonciani *et al.*, Nucl. Phys. **B529**, 424 (1998).

[6] N. Kidonakis and R. Vogt, Phys. Rev. D **68**, 114014 (2003).

[7] M. Cacciari *et al.*, J. High Energy Phys. 04 (2004) 68.

[8] V. Abazov *et al.* (D0 Collaboration), Phys. Lett. B **626**, 35 (2005); **626**, 45 (2005); **626**, 55 (2005).

[9] D. Acosta *et al.* (CDF Collaboration), Phys. Rev. D **71**, 052003 (2005); **72**, 032002 (2005); **71**, 072005 (2005); D. Abulencia *et al.* (CDF Collaboration), Phys. Rev. Lett. **97**, 082004 (2006).

[10] B. Abbott *et al.* (D0 Collaboration), Phys. Rev. Lett. **82**, 4975 (1999).

[11] J. F. Gunion *et al.*, *The Higgs Hunters Guide* (Addison-Wesley, Reading, MA, 1990), p. 200; V. Abazov *et al.* (D0 Collaboration), Phys. Rev. Lett. **92**, 221801 (2004); T. Affolder *et al.* (CDF Collaboration), Phys. Rev. Lett. **96**, 042003 (2005).

[12] H. P. Nilles, Phys. Rep. **110**, 1 (1984); H. J. He, N. Poleonsky, and S. Su, Phys. Rev. D **64**, 053004 (2001); V. A. Novikov, I. B. Okun, A. N. Rozanov, and M. I. Vyosotsky, Phys. Lett. B **529**, 111 (2002); D. Choudhury, T. M. P. Tait, and C. E. M. Wagner, Phys. Rev. D **65**, 053002 (2002); H. Cheng and I. Low, J. High Energy Phys. 309 (2003) 51.

[13] V. Abazov *et al.* (D0 Collaboration), Nucl. Instrum. Methods Phys. Res., Sect. A **565**, 463 (2006).

[14] V. Abazov *et al.* (D0 Collaboration), Nucl. Instrum. Methods Phys. Res., Sect. A **552**, 372 (2005).

[15] T. Andeen *et al.*, FERMILAB Report No. FERMILAB-TM-2365.

[16] R. E. Kalman, J. Basic Eng. **82**, 35 (1960).

[17] W. M. Yao *et al.*, J. Phys. G **33**, 1 (2006).

[18] G. C. Blazey *et al.*, in *Proceedings of the Workshop: QCD and Weak Boson Physics in Run II*, edited by U. Baur, R. K. Ellis, and D. Zeppenfeld (Fermilab Report No. Fermilab-Pub-00/297, 2000).

[19] V. Abazov *et al.* (D0 Collaboration), Phys. Rev. D **75**, 092001 (2007).

[20] M. L. Mangano *et al.*, J. High Energy Phys. 07 (2003) 001.

[21] T. Sjöstrand *et al.*, Comput. Phys. Commun. **135**, 238 (2001).

[22] S. Alekhin *et al.*, arXiv:hep-ph/0204316.

[23] D. Stump *et al.*, J. High Energy Phys. 10 (2003) 046.

[24] D. J. Lange, Nucl. Instrum. Methods Phys. Res., Sect. A **462**, 152 (2001).

[25] R. Brun and F. Carminati, CERN program library long writeup Report No. W5013, 1993.

[26] V. Abazov *et al.* (D0 Collaboration), Phys. Rev. D **74**, 112004 (2006).

[27] V. Abazov *et al.* (D0 Collaboration), Phys. Rev. D **76**, 052006 (2007).

[28] B. Abbott *et al.* (D0 Collaboration), Phys. Rev. D **58**, 052001 (1998).

[29] V. Barger, J. Ohnemus, and R. J. N. Phillips, Phys. Rev. D **48**, R3953 (1993).

[30] F. Tkachev, Int. J. Mod. Phys. A **12**, 5411 (1997), and private communication.